

Coherent electron transport in quasi one-dimensional carbon-based systems

I. Deretzis and A. La Magna^a

Consiglio Nazionale Delle Ricerche, Istituto per la Microelettronica e Microsistemi, Z. I. VIII Strada 5, 95121, Catania, Italy

Received 23 February 2011 / Received in final form 21 March 2011

Published online 4 May 2011 – © EDP Sciences, Società Italiana di Fisica, Springer-Verlag 2011

Abstract. This Colloquium discusses the coherent electron transport properties of non-ideal quasi-one-dimensional carbon-based systems, i.e. graphene nanoribbons, carbon nanotubes and linear chains. Results are based on numerical simulations that implement Schrödinger/Poisson as well as non-equilibrium polaronic methodologies for the calculation of quantities relative to the conduction. Attention is paid on the role of localized or extended modifications of the structural and electronic symmetry within atomistic descriptions that go beyond phenomenological approaches. Three different types of perturbations are considered: (a) perturbations induced by defects/impurities in the atomic lattice, (b) perturbations induced by the coupling with the metallic contacts, and (c) perturbations induced by the application of bias. The objective is to elucidate the potentiality as well as the possible drawbacks of future all-carbon-based electronics.

1 Introduction

Silicon-based complementary-metal-oxide semiconductor (CMOS) technology has ruled the semiconductor industry for the last decades. However, pure silicon electronics is arriving toward its physical limits in terms of traditional transistor operation: as channel lengths get reduced below $L_{ch} \sim 30\text{--}20$ nm, strong differentiations in the device operation are expected due to the presence of quantum confinement, while problems like leakage currents and dielectrics scaling arise¹. In this sense the search of alternative materials and/or device architectures for nanoscale integration in electronics that would allow for a further reduction of transistor dimensions, while at the same time increasing clock speeds and reducing power dissipation becomes eminent. Such research could also boost the development of sensors, environmental and in general smart applications, where old and new functionalities are integrated into the same chip. A new concept of low-dimensional systems and/or materials comes into the picture here. Reduced dimensionality can significantly advance miniaturization and improve performance: devices become faster, denser and require lower power consumption. Hence, plenty of potential innovative features could be achieved if one or more of the space dimensions of the material used for manufacturing electronic devices were intrinsically zero. Under this perspective, novel carbon-based systems play a key role.

1.1 Low-dimensional carbon-based systems

Using zero-dimensional materials (i.e. molecules or atoms) as electronic building blocks, i.e. pushing the low dimensionality concept to an extreme limit, is not a recent proposal [1]. However, the real revolution in low-dimensional electronics came with the discovery of carbon nanotubes (CNTs) [2], i.e. quasi one-dimensional (1D) sp^2 -bonded carbon allotrope systems that look like a single rolled sheet of graphite. The CNT research framework [3,4] served for the incubation of the concept of a pure two-dimensional (2D) carbon-based system. Quasi-2D electron gases exist in heterostructure junctions like the GaN/AlGaIn interface. Anyhow, the idea of a real 2D material was lacking any consistence whereas serious thermodynamic stability concerns were raised [5,6]. In 2004 Novoselov et al. [7] showed the existence and stability of a 2D crystal comprising of a single one-atom-thick graphite sheet with a series of exceptional properties: graphene is indeed the strongest and most conductive material ever synthesized [8].

Out of the plethora of electronic characteristics that could make graphene an ideal candidate for post-Si CMOS technology there is still one missing, i.e. the intrinsic bandgap that could allow for its direct use as an active component in semiconducting devices. The proposed solutions for the non-trivial bandgap engineering problem include: (a) the lateral confinement of graphene in one dimension, i.e. the mechanical transformation from a quantum well to a quantum wire [9]. (b) The synthesis of Bernal-stacked bilayer graphene systems, where it has been shown that the application of a perpendicular electric field (e.g. by using a gate electrode) can give rise to a

^a e-mail: antonino.lamagna@imm.cnr.it

¹ International technology roadmap for semiconductors, <http://www.itrs.net/>

small (~ 0.2 eV) bandgap [10,11]. (c) The interaction between graphene and a substrate [12,13]. (d) The chemical functionalization of bilayer graphene with reactive atoms or molecules [11,14]. (e) The generation of mobility gaps within a backscattering mechanism from defects and substitutional impurities during conduction [15,16]. (f) The introduction of controlled strain fields [17,18]. While all the mentioned methodologies have advantages and disadvantages, a most plausible route toward bandgap engineering within a current view of technological advances, which guarantees device-requested functionality, appears to be the one of 1D confinement: the controlled production of quasi-one-dimensional graphene, either in the form of a flat sheet (i.e. a graphene nanoribbon (GNR)) or in that of a rolled wire (i.e. a CNT), with all enhancements made possible by surface chemistry, strain and substrate engineering.

In addition, carbon's vast polymorphism allows for research of low-dimensional systems beyond the sp^2 scheme. Indeed, strictly one dimensional carbon allotropes in the sp hybridization (i.e. dimerized polyynic carbon chains or un-dimerized cumulene carbon chains) have been synthesized before of their sp^2 counterparts [19] and recently inside multiwall CNTs [20]. In spite of their relative instability, these molecules appear as ideal candidates for molecular electronics since they possess all the necessary features: tunable band gap (by modifying the polyynic's chain size), high conductivity, metal and semiconductor character in the same molecular structure [21].

1.2 Coherent transport: role of defects, contacts and bias

All carbon-based quasi-one dimensional systems mentioned in the previous subsection expose an one-atom-thick surface and as a consequence their properties are deeply subjected to the interaction with the surrounding environment. This interaction is bound to induce various levels of disorder in these materials. Already from the growth stage and notwithstanding the possibility to obtain high crystalline quality at the micrometer scale, all popular growth techniques for graphene and CNTs give rise to local or extended deviations from the ideal atomic structure (e.g. vacancies, Stone-Wallles defects, etc. [22]). A further source of structural disarrangement can be identified within patterning manipulations. Finally the steps of device integration for these structures enhance perturbations and interactions with both dielectrics and contacts, giving rise to important alterations in their conductance characteristics [23].

The theoretical understanding of disorder on the conductance features of these systems and in general the study of the coherent transport represents a fundamental background to develop carbon-based nanoelectronics. This issue complements the studies on diffusive transport and it is crucial for predicting the electrical characteristics in the case of nano-device configurations: i.e. when the device length scale is lower than the characteristic lengths of inelastic interactions that give rise to a diffusive behavior or the de-phasing of the electron wave functions.

Under this perspective the use of phenomenological approaches (e.g. the Anderson model [24]) for the inclusion of disorder in electronic transport properties of carbon-based systems [25] serves as a first approximation in the macroscale, but lack authoritativeness for the effects of local atomic reconstruction at the disordered area. The presence of defects and/or impurities, the interface with a particular substrate, the interaction with a metallic contact, the charge transfer induced by a local perturbation and in general all the structural/electronic deviations from the ideal case need an atomistic-level description. It is therefore clear that a thorough understanding of different types of deviations from the ideal atomic/electronic structure, as well as their role in the shaping of the transport properties of carbon-based quasi-1D systems is of a fundamental importance. The goal of this Colloquium is to discuss the role of non-ideality on the electronic transport properties of carbon-based nanowires. Three different types of atomic/structural and electronic perturbations will be considered: (a) perturbations induced by defects and impurities in the atomic lattice, (b) perturbations induced by the coupling with the metallic contacts, and (c) perturbations induced by the application of bias.

We finish this introductory section with the plan of the Colloquium's technical content. Section 2 contains a basic presentation of the electronic structure of GNRs, CNTs and carbon chains in their ideal configuration. Section 3 introduces a general formalism for the calculation of coherent electron transport in nanodevices. Section 4 discusses the quantum transport modeling of defective sp^2 systems, from the effect of the single scatterer all the way up to finite defect concentrations. Section 5 analyses the implications on the conductance induced by the interaction between metallic contacts and CNT/GNR structures, paying attention on both the chemical aspects of the interface bonding as well as the particularity of the one-dimensional electrostatics. Section 6 treats polaronic effects in carbon chains that manifest in the presence of a bias voltage. Finally, in Section 7 conclusions are presented along with a discussion and a general outlook.

2 Electronic structure of ideal carbon nanosystems

In this section we review the basic features of the electronic structure for some carbon-based low dimensional systems. In the case of ideal bulk structures, the single-orbital tight-binding (TB) approximation is sufficient for most of the relevant aspects of the band structure. Moreover, it allows to obtain fully analytic results or to reduce the computational cost at a minimum. In this section TB results will be derived and discussed; however, the corrections obtained by means of more accurate approaches will be also outlined.

2.1 Graphene: a two-dimensional world

In spite of its more recent synthesis, graphene can be conceptually considered as the parent-material for most of the nano-systems that are studied in this Colloquium: curiously, carbon nano-tubes, -balls, etc. were discovered

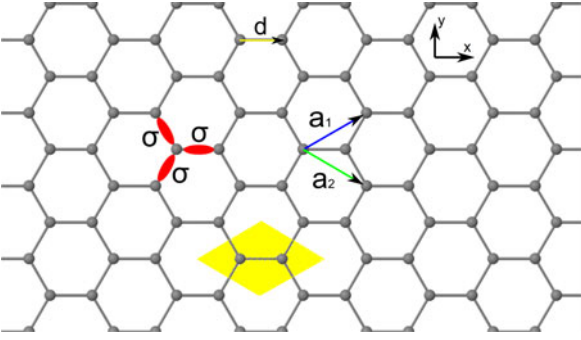


Fig. 1. The atomic structure of a graphene surface where $\mathbf{a}_1, \mathbf{a}_2$ are lattice vectors, \mathbf{d} is the vector joining the two atoms in the elementary cell and σ are the sp^2 -hybridized bonds that allow for the covalent bonding between neighboring atoms. The unit cell is highlighted in yellow.

before their constituent foils. Here instead, we will start this section with a view of the electronic properties of the 2D crystal.

Graphene is a one-atom thick planar sp^2 carbon allotrope system with particular electrical, mechanical and optical characteristics [8,26,27]. Structurally graphene is a hexagonal honeycomb surface where each carbon atom is covalently bonded with three neighbouring atoms at a distance $d \simeq 1.42 \text{ \AA}$ (see Fig. 1). The primitive basis vectors of the underlying Bravais lattice read:

$$\mathbf{a}_1 = \frac{a}{2} (\sqrt{3}, 1) \quad (1)$$

$$\mathbf{a}_2 = \frac{a}{2} (\sqrt{3}, -1) \quad (2)$$

where $\mathbf{a}_1, \mathbf{a}_2$ are lattice vectors and a is the in-plane graphite lattice constant, having a value of $a = \sqrt{3}d \simeq 2.46 \text{ \AA}$. Since the translation of each one of the basis vectors gives rise to a hexagonal primitive lattice, graphene can be thought of as the superposition of two hexagonal interpenetrating lattices.

The sp^2 hybridization scheme provides for the presence of both σ and π orbitals in the electronic structure of this system. The σ orbitals primarily lie along the structure's surface and are responsible for covalent bonding between neighboring C atoms that constitutes the basis of the extremely high mechanical stability of this material (see Fig. 1). On the other hand σ bonds have energies that are too far away from the Fermi level and do not contribute in the electrical characteristics of graphene. The remaining π orbitals (one per carbon atom) lie perpendicular to the lattice surface and are responsible for the peculiarity of its low-energy electronic properties.

Probing for the electronic structure of graphene can be simple and straightforward within a next-neighbor TB model. Such a description accounts only for the linear combination of π atomic orbitals of graphene, being sufficient for the low-energy spectrum of this material. We start from the next-neighbor TB Hamiltonian:

$$H = -t \sum_{\langle i,j \rangle, \sigma} c_{i,\sigma}^\dagger c_{j,\sigma} + h.c., \quad (3)$$

where $c_i(c_i^\dagger)$ is the annihilation (creation) operator for an electron with spin σ at site i , and t is the hopping integral with a typical value $t = 2.7 \text{ eV}$. The previous Hamiltonian can be rewritten with a notation that introduces the bipartite nature of the honeycomb lattice [28]:

$$H = -t \sum_{n,m,\sigma} c_{n,m,\sigma}^{(1)\dagger} \left(c_{n,m,\sigma}^{(2)} + c_{n+1,m,\sigma}^{(2)} + c_{n,m+1,\sigma}^{(2)} \right) + h.c., \quad (4)$$

where operator $c^{(1)}(c^{(1)\dagger})$ is the annihilation (creation) operator at sublattice $\mathbf{L}_{n,m} = n\mathbf{a}_1 + m\mathbf{a}_2$, and $c^{(2)}(c^{(2)\dagger})$ is the annihilation (creation) operator at sublattice $\mathbf{L}_{n,m} = n\mathbf{a}_1 + m\mathbf{a}_2 + \mathbf{d}$. By Fourier transforming in momentum space we get:

$$b_{\mathbf{k},\sigma}^{(1)} = \frac{1}{\sqrt{N_s}} \sum_{n,m,\sigma} e^{i\mathbf{k} \cdot \mathbf{L}_{n,m}^{(1)}} c_{n,m,\sigma}^{(1)} \quad (5)$$

$$b_{\mathbf{k},\sigma}^{(2)} = \frac{1}{\sqrt{N_s}} \sum_{n,m,\sigma} e^{i\mathbf{k} \cdot \mathbf{L}_{n,m}^{(2)}} c_{n,m,\sigma}^{(2)} \quad (6)$$

$$c_{n,m,\sigma}^{(1)} = \frac{1}{\sqrt{N_s}} \sum_{\mathbf{k},\sigma} e^{-i\mathbf{k} \cdot \mathbf{L}_{n,m}^{(1)}} b_{\mathbf{k},\sigma}^{(1)} \quad (7)$$

$$c_{n,m,\sigma}^{(2)} = \frac{1}{\sqrt{N_s}} \sum_{\mathbf{k},\sigma} e^{-i\mathbf{k} \cdot \mathbf{L}_{n,m}^{(2)}} b_{\mathbf{k},\sigma}^{(2)} \quad (8)$$

where \mathbf{k} is the electron quasi-momentum and N_s is the number of unit cells in the graphene sheet. Substituting back to (4) we get:

$$H = -t \sum_{\mathbf{k},\sigma} e^{-i\mathbf{k} \cdot \mathbf{d}} (1 + e^{-i\mathbf{k} \cdot \mathbf{a}_1} + e^{-i\mathbf{k} \cdot \mathbf{a}_2}) \cdot b_{\mathbf{k},\sigma}^{(1)\dagger} \cdot b_{\mathbf{k},\sigma}^{(2)} + h.c.$$

The energy dispersion relation can be derived from the previous Hamiltonian by means of a Bogoliubov transformation:

$$H = \pm \sum_{\mathbf{k},\sigma} E(\mathbf{k}) \cdot \tilde{b}_{\mathbf{k},\sigma}^\dagger \cdot \tilde{b}_{\mathbf{k},\sigma} \quad (9)$$

with

$$E(\mathbf{k}) = t [3 + 2 \cos(\mathbf{k} \cdot \mathbf{a}_2) + 2 \cos(\mathbf{k} \cdot \mathbf{a}_1) + 2 \cos(\mathbf{k} \cdot (\mathbf{a}_2 - \mathbf{a}_1))]^{1/2} \quad (10)$$

where $\tilde{b}_{\mathbf{k},\sigma}$ is a linear combination of $b_{\mathbf{k},\sigma}^{(1)}$ and $b_{\mathbf{k},\sigma}^{(2)}$. By projecting the previous expression on the graphene plane we have:

$$E(k_x, k_y) = \pm t \times \sqrt{1 + 4 \cos^2 \left(\frac{k_y a}{2} \right) + 4 \cos \left(\frac{k_y a}{2} \right) \cos \left(\frac{k_x \sqrt{3} a}{2} \right)}, \quad (11)$$

where k_x, k_y are wavevector components along the x, y directions (see Fig. 2). According to equation (11), valence and conduction bands meet exactly at the charge neutrality level at the high symmetry K and K' points of the Brillouin zone. Such a band formation gives rise to a

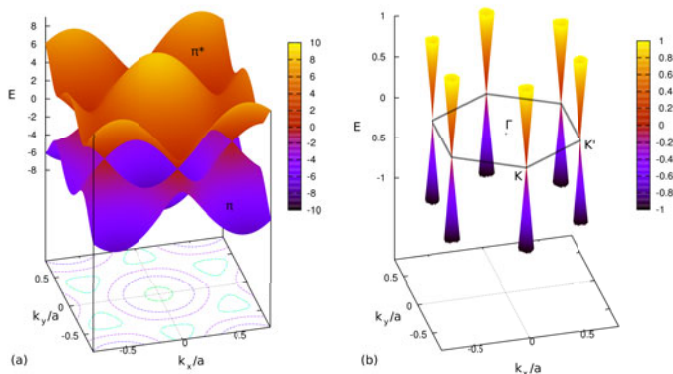


Fig. 2. (a) Energy dispersion relation of two-dimensional graphene for the π and π^* bands according to the single-orbital TB model. (b) Detail of the energy dispersion relation of two-dimensional graphene showing band meeting at the high symmetry K and K' points of the first Brillouin zone.

density of states that vanishes linearly at the Fermi level making graphene a half-filled zero-gap semiconductor.

The peculiarity of the band structure of graphene lies in the linear dispersion near the Fermi level (see Fig. 2b) where electrons behave like Dirac massless chiral quasi-particles (relativistic fermions), making graphene an ideal platform for the experimental study of quantum electrodynamics phenomena. Indeed, for the low energy spectrum the dispersion relation reads:

$$H(\mathbf{k}) = \pm \hbar \nu_F \begin{pmatrix} 0 & k_x - ik_y \\ k_x + ik_y & 0 \end{pmatrix} = \pm \hbar \nu_F \boldsymbol{\sigma} \cdot \mathbf{k},$$

where \mathbf{k} is the quasi-particle momentum, $\boldsymbol{\sigma}$ are the 2D Pauli matrices and $\nu_F (\approx 10^6 \text{ m s}^{-1})$ is the Fermi velocity. It should be noted that the use of the Dirac-like Hamiltonian is valid only for a small part of the energy spectrum ($|E| < \sim 1 \text{ eV}$) of 2D graphene, while it lacks sense for higher energies or other forms of confined graphene systems.

The electronic properties of graphene form the cornerstone of its physical peculiarity, giving rise to the manifestation of a series of exceptional phenomena and device-requested characteristics (e.g. huge charge carrier density and mobility, extreme mechanical strength, etc. [8]). On the other hand, an intrinsic bandgap can be only obtained with the further confinement of one out of its two dimensions.

2.2 Tube confinement

The carbon nanotube geometry is characterized uniquely by the circumferential (chiral) vector $\mathbf{C} = n\mathbf{a}_1 + m\mathbf{a}_2 \equiv (n, m)$ with $(0 \leq |m| \leq n)$ connecting two equivalent lattice points in the ideal wrapping of a planar graphene ribbon in the tubular form. Such vector imposes real periodic boundary conditions in the 2D structure and constrains the allowed values of \mathbf{k} . Note here that (n, n) CNTs have armchair borders (aCNTs from now on) whilst $(n, 0)$ CNTs have zig-zag borders (zCNTs from now on). Thanks

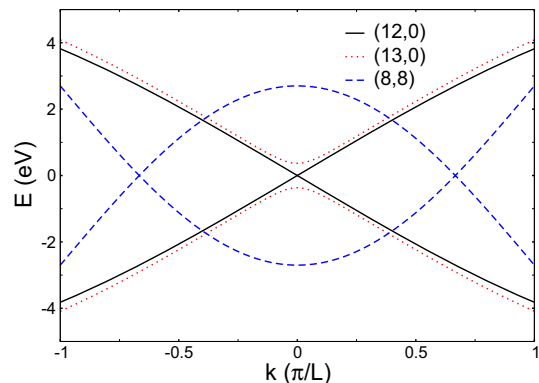


Fig. 3. Energy dispersion relation showing the highest occupied and the lowest unoccupied subbands of (a) a (12, 0) zCNT, (b) a (13, 0) zCNT and (c) a (8, 8) aCNT according to the zone-folding model.

to the circular symmetry, the band-structure of a CNT in the TB approximation can be easily obtained from the graphene one within the zone folding approximation. Indeed, the proper quantization rule for the wave vector in this geometry can be derived from the 2D k_x, k_y ones imposing the following relation

$$\mathbf{C} \cdot \mathbf{k} = k_x C_x + k_y C_y = 2\pi p, \quad (12)$$

where p is an integer number. Equation (12) is a constrain between (k_x, k_y) in terms of a family of parallel lines whose points represent the tube wave numbers. An immediate but important consequence at the quantization condition (12) is that CNTs are metallic or semiconducting, depending on whether or not the lines pass through the graphene Fermi points [29]. From this geometrical rule it follows that CNTs are metallic if $\text{mod}(n-m, 3) = 0$. We can find an analytical expression of CNT band structure by expressing the constrained k_x, k_y values as a function of the component k of the tube wave vectors parallel to the axis. By substituting these expressions in equation (11), we finally obtain

$$E(p, k) = \pm t \left[1 + 4 \cos^2 \left(\frac{\sqrt{3} C_y k a}{2C} + \frac{\sqrt{3} \pi p C_x a}{C^2} \right) + 4 \cos \left(\frac{3 C_x k a}{2C} - \frac{3 \pi p C_y a}{C^2} \right) \cos \left(\frac{\sqrt{3} C_y k a}{2C} + \frac{\sqrt{3} \pi p C_x a}{C^2} \right) \right]^{1/2} \quad (13)$$

The band structure of CNTs according to the zone-folding approximation (see Fig. 3) is revised within higher-order models that account for the effects of curvature and orbital mixing on the electronic structure. The principal qualitative differences are two: (a) the TB description is inadequate for small radius CNTs [30], and (b) a small bandgap opens in the case of the metallic zigzag and chiral CNTs [31], perturbing the ideal linearity of the dispersion relation around the Fermi point.

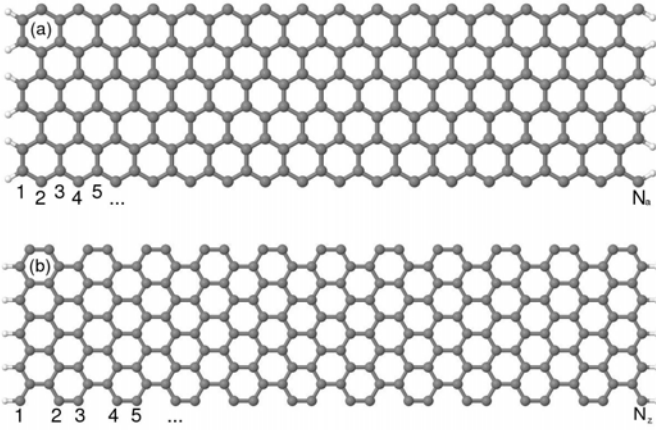


Fig. 4. GNRs with armchair (a) and zigzag (b) edges passivated by single hydrogens. The respective categorization can take place on the basis of the dimer lines N_a and zigzag chains N_z along the ribbon width.

2.3 Ribbon confinement

Contrary to the tube confinement, the band structure of graphene ribbons for a generic geometry cannot be analytically calculated. It is noteworthy that numerical calculations of GNR band structures were present in the literature well before the graphene synthesis [32,33], while a systematic study of the GNR band structure within an *ab initio* framework can be found in reference [9]. However, analytical band structure expressions can be derived for the particular case of ribbons with armchair edges (see Fig. 4a), whilst in spite of the simplicity of the edge shape in the zig-zag symmetry (Fig. 4b) a numerical approach is necessary.

2.3.1 Armchair ribbon confinement

Armchair graphene nanoribbons (aGNRs) are quasi-1D graphene-based structures, where the lateral confinement consists of left/right terminated armchair edges. Prevailing definition enumerates the number of dimer lines N_a along the ribbon width [9] (see Fig. 4a). Probing for the electronic properties of ideal aGNRs can take place analytically within the TB schema of equation (3) by considering appropriate boundary conditions towards the width of these structures that nullify the wave function out of the structure's borders [34]:

$$q_y = \frac{2}{a} \frac{p\pi}{N_a + 1}, \quad (14)$$

where q_y is the discretised vector in the y direction and $p = 1, 2, 3, \dots, N_a$. Hamiltonian diagonalization here gives the following dispersion relation:

$$E(k_x, q_y) = \pm t \left| 2e^{\frac{ik_x a}{2\sqrt{3}}} \cos \frac{aq_y}{2} + e^{\frac{-ik_x a}{\sqrt{3}}} \right|. \quad (15)$$

A key characteristic of the TB band structure of aGNRs is its dependence on the number of dimer lines according

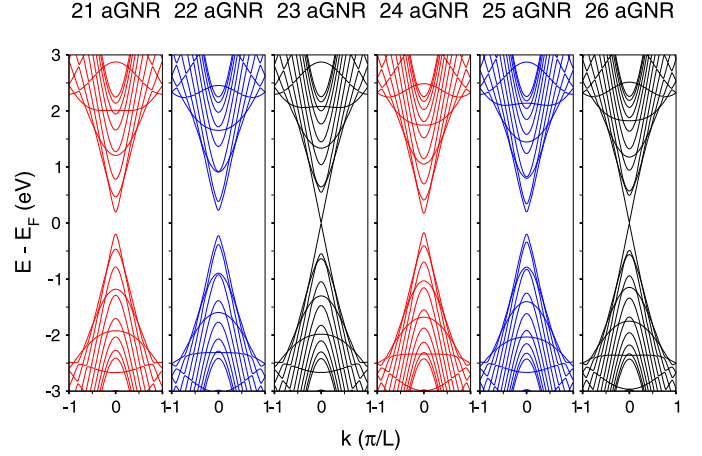


Fig. 5. Energy dispersion relation of aGNRs within the extended Hückel theory for six different dimer line widths ($N_a = 21-26$). Model parameters have been extrapolated from first-principles calculations. L is the lattice periodicity.

to the following rule: $\forall p \in N$, aGNRs with $N_a = 3p + 2$ dimer lines are metallic while the rest are semiconducting with energy gaps Δ given by the following equations [27]:

$$\Delta_{3p} = |t| \left(4 \cos \frac{\pi p}{3p+1} - 2 \right) \quad (16)$$

$$\Delta_{3p+1} = |t| \left(2 - 4 \cos \frac{\pi(p+1)}{3p+2} \right). \quad (17)$$

The previous picture is slightly revised when the electronic Hamiltonian is written beyond nearest-neighbor interactions and with the inclusion of edge effects towards the uplifting of metallicity and the formation of secondary band gaps (of the order of few meV) for aGNRs with $N_a = 3p + 2$ dimer lines (see Fig. 5 for the band structure of aGNRs according to a description that considers further-neighbor interactions as well as σ orbitals).

2.3.2 Zigzag Ribbon confinement

Zigzag graphene nanoribbons (zGNRs) (see Fig. 4) are quasi-1D graphene-based structures identified by the number of zigzag chains N_z along the ribbon width that always have their two edge carbon atoms belonging to the different sublattices A and B (see Eq. (4)). This characteristic makes the imposition of boundary conditions that nullify the wave function at the borders separate according to a reciprocal scheme where the wave function of sublattice A vanishes at the opposite B -type edge and vice-versa [27]. An analytical expression for the dispersion relation in zGNRs is not possible, however the numerical diagonalization of the Fourier-transformed $N_t \times N_t$ blocks of the nearest-neighbor TB Hamiltonian yields a band structure that presents some important characteristics: the Dirac points of two-dimensional graphene are projected at the $k = \pm \frac{2\pi}{3}$ points of the first 1D Brillouin

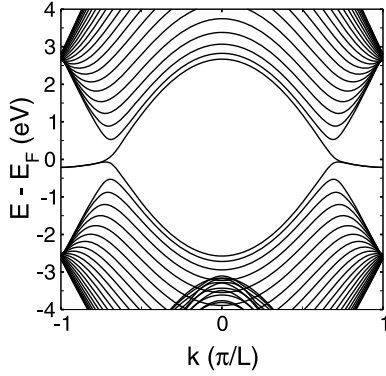


Fig. 6. Energy dispersion relation of a 22-zGNR ($N_z = 22$) within the extended Hückel theory. L is the lattice periodicity.

zone, and b) from $k = \pm \frac{2\pi}{3}$ to $k = \pm\pi$, i.e. until the borders of the Brillouin zone there exist two partially flat degenerate bands with zero energy. The revisions in the previous picture imposed by higher order Hamiltonians show that the two degenerate subbands near the borders of the Brillouin zone slightly bend towards negative energies and do not maintain a zero value (see Fig. 6). A further inclusion of exchange interactions shows that the highly localized wave function at the edges of the zGNR around the charge neutrality point gives rise to a ferromagnetic/antiferromagnetic coupling, which opens a small meV bandgap in between the two quasi degenerate subbands [9]. This last characteristic has driven a wide discussion on the possibility of spin-related phenomena based on the zigzag edges of GNRs (i.e. zGNRs as spintronic systems). However it should be noted that some of the conditions of suppression for edge magnetism are the presence of edge corrugation [35], polihydrogenation of the edge atoms [36] and room temperatures [37], which are all likely to be met in real GNR samples.

2.4 Carbon chains

With respect to the quasi-1D nature of CNTs and GNRs, polyynic and cumulenic chains, i.e. dimerized and non-dimerized chains of carbon atoms respectively, present a truly 1D character. Carbon chains distinguish themselves from their quasi-1D counterparts also in their chemical bonding characteristics, where an sp rather than sp^2 hybridization takes place. However, their presence and stability is related to CNTs, as recent arc discharge multiwall CNT synthesis has shown [20].

The key issue for the theoretical understanding of these chain systems is the instability of the highly symmetric configuration (i.e. the cumulene structure where the carbon atoms in the chain form equivalent bonds with next-neighbour atoms) with respect to a configuration (polyyne) showing Bond Length Alternation (BLA), i.e. alternation of stronger (triple) and weaker (single) bonds. The band gap of the polyyne is strongly related to the BLA, as stated in the Peierls theorem [38], whilst the cumulene has a metallic character. Thermal driven reversible

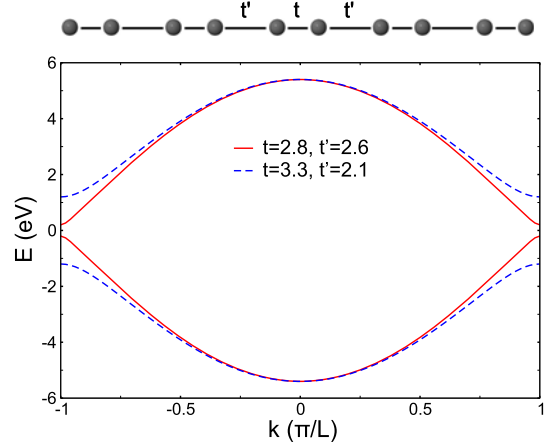


Fig. 7. Energy dispersion relation for a dimerized carbon chain for two different configurations of the hopping integrals t and t' . L is the lattice periodicity.

transition between the polyynic and the cumulenic configuration has been recently observed [39] indicating the reliability of the Peierls transition scenario.

A reliable effective Hamiltonian, for modelling the electronic structure of a chain of N carbon atoms, is a modified Su-Schrieffer and Heeger (SSH) model with two degenerate orbitals per site. The model [40] reads

$$\begin{aligned}
 H[u_n] = & -t_0 \sum_{n,l,\sigma} c_{n+1,l,\sigma}^\dagger c_{n,l,\sigma} + c_{n,l,\sigma}^\dagger c_{n+1,l,\sigma} \\
 & + \alpha \sum_{n,l,\sigma} (u_{n+1} - u_n) \left[c_{n+1,l,\sigma}^\dagger c_{n,l,\sigma} c_{n,l,\sigma}^\dagger + c_{n+1,l,\sigma} \right] \\
 & + \sum_n p_n^2 / 2M + (u_{n+1} - u_n)^2 \quad (18)
 \end{aligned}$$

where $c_{n,l,\sigma}^\dagger$, $(c_{n,l,\sigma})$ is the creation (annihilation) operator of an electron with spin σ , u_n is the dimerization coordinate, p_n the conjugated momentum, $t_0 = 2.7$ eV is the hopping integral between carbons and α the electron-phonon coupling energy. A negligible mass parameter $1/M$ is assumed (adiabatic approximation). In the case of an infinite chain, the ground state energy as a functional of $[u_n]$ can be analytically evaluated, assuming $u_n = (-1)^{n-1} u_0$ and diagonalizing the resulting Hamiltonian in the momentum space (considering two atoms per elementary cell as in 2.1) again by means of a Bogoliubov transformation:

$$E(k) = \epsilon \pm \sqrt{t^2 + t'^2 + 2tt' \cos(kL)}, \quad (19)$$

where $t = t_0 + 2\alpha u_0$, $t' = t_0 - 2\alpha u_0$ and L is the lattice periodicity. The interesting aspect of the electronic structure of these systems lies in the possibility to tune their conducting characteristics by changing the distance between the neighboring atoms, e.g. by the modification of the $BLA = 4u_0$ value (see Fig. 7 for two different configurations of the hopping parameters).

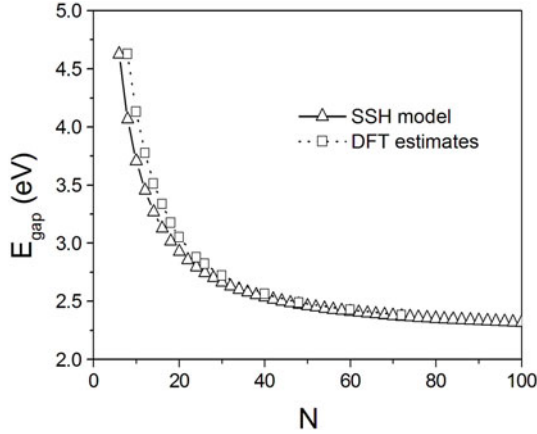


Fig. 8. HOMO-LUMO gap as a function of the size N for a dimerized carbon chain derived by means of the modified SSH model (triangles) and ab-initio calculations (squares)

The best variational choice of u_0 can be obtained minimizing the energy functional. This procedure allows to calibrate the parameters for the model imposing that the calculated BLA and band gap Δ coincide with the best estimates ($BLA = 0.013$ nm, $\Delta = 2.2$ eV) derived by means of a critical analysis based on quantum chemistry calculations using different hybrid density functional theories (DFTs) [41]. The calibration procedure gives $\alpha = 8.46$ eV/Å and $K = 137.1$ eV/Å². For finite chains with an even number of atoms N , the BLA and the gap can be calculated numerically assuming the same ansatz for u_n and minimizing the energy functional. These gap values obtained are reported in Figure 8 and compared to the DFT estimate as a function of N . In spite of the fact that no size dependent calibration is performed, there is a good agreement between the DFT (squares) and the model (triangle) estimates in a large range of N .

3 Quantum transport theory

This section will present some keynotes on a quantum transport formalism for problems that diffusive and semi-classical models fail to address. This model is a combination of the single-particle scattering theory using Green's function techniques with the Landauer derivation for the transmission probability and the current. The power of such purely quantistic theory lies in its capacity to additionally describe systems where transport is phase coherent. This conduction regime is prevalent for a number of nanoscale materials like graphene (up to a sub-micrometer limit), carbon nanotubes, polyynes and other organic/inorganic molecules.

3.1 Green's function

The Green's function technique represents a convenient formalism to separate the part of the Hamiltonian (often

the interaction part) which does not allow a direct, possibly analytical, solution of the quantum problem in study. A rigorous and complete introduction of the formalism is beyond the scope of this Colloquium. Here we will specialize the approach for the case where the interaction part is due to the presence of contacts between a finite (solvable by analytical or numerical techniques) and an infinite system.

We consider the generalized transport problem of a two-terminal geometry, where a finite device part is embedded between semi-infinite left and right contacts, which do not interact directly. Assuming that a matrix representation of the Hamiltonian can be obtained using a suitable base, we can write the Hamiltonian of the entire system as [42]:

$$H = \begin{pmatrix} H_L & -\tau_L & 0 \\ -\tau_L^\dagger & H_0 & -\tau_R^\dagger \\ 0 & -\tau_R & H_R \end{pmatrix}. \quad (20)$$

Here, H_0 is the device Hamiltonian and $H_{L,R}$ are the bulk contact Hamiltonians, while $\tau_{L,R}$ describe the coupling between contacts and device. In this way, although contact subspaces are semi-infinite, the device subspace has a finite character. The Green function of the system represents the response in one point of a conductor that takes place in a different point of the same conductor. Conceptually it is related to the scattering matrix (S-matrix) [24], albeit its applicability is more general and powerful. The matrix Green function \mathcal{G} can be defined by the solutions to the following formal equation

$$(EI - H)\mathcal{G}(E) = I \quad (21)$$

where E is the energy and I is the unitary matrix (in the case of an orthonormal basis set). Equation (21) gives in fact two equivalent solutions, which are called the advanced (\mathcal{G}^A) and the retarded (\mathcal{G}^R) Green's functions and physically represent an incoming and an outgoing wave that are formed due to the same excitation. Mathematically we can obtain only one solution by imposing correctly the boundary conditions, which in our case is translated in adding or subtracting an infinitesimal imaginary part to the energy. It is also straightforward to show that $(\mathcal{G}^R)^\dagger = \mathcal{G}^A$.

We can separate the Green's function that corresponds to the device (\mathcal{G}_0) and the contacts ($\mathcal{G}_{L,R}$), and by substituting to equation (21) we have:

$$\begin{pmatrix} EI - H_L & -\tau_L & 0 \\ -\tau_L^\dagger & EI - H_0 & -\tau_R^\dagger \\ 0 & -\tau_R & EI - H_R \end{pmatrix} \begin{pmatrix} \mathcal{G}_L & \mathcal{G}_{L0} & \mathcal{G}_{LR} \\ \mathcal{G}_{0L} & \mathcal{G}_0 & \mathcal{G}_{0R} \\ \mathcal{G}_{RL} & \mathcal{G}_{R0} & \mathcal{G}_R \end{pmatrix} = \begin{pmatrix} I & 0 & 0 \\ 0 & I & 0 \\ 0 & 0 & I \end{pmatrix}.$$

Considering matrix multiplications with the second column of the Green matrix, we obtain the following set of equations:

$$(EI - H_L) \mathcal{G}_{L0} - \tau_L \mathcal{G}_0 = 0 \quad (22)$$

$$-\tau_L^\dagger \mathcal{G}_{L0} + (EI - H_0) \mathcal{G}_0 - \tau_R^\dagger \mathcal{G}_{R0} = I \quad (23)$$

$$(EI - H_R) \mathcal{G}_{R0} - \tau_R \mathcal{G}_0 = 0. \quad (24)$$

In this set (22) and (24) give matrices with (∞, N) dimensions, whereas (23) has (N, N) dimensions, where N is the dimension of the device Hamiltonian written in an appropriate basis set. If we solve for \mathcal{G}_{L0} and \mathcal{G}_{R0} we have:

$$\mathcal{G}_{L0} = (EI - H_L)^{-1} \tau_L \mathcal{G}_0 = g_L \tau_L \mathcal{G}_0 \quad (25)$$

$$\mathcal{G}_{R0} = (EI - H_R)^{-1} \tau_R \mathcal{G}_0 = g_R \tau_R \mathcal{G}_0, \quad (26)$$

where $g_{L,R}$ are the Green functions of the left and right contact respectively. The problem here is the transformation of these two (∞, N) matrices into (N, N) ones for substitution back to equation (23) in order to obtain a finite expression. Such a procedure usually takes advantage of the semi-infinite lattice symmetry of the two leads in order to make a k -space transformation of the real-space matrices $g_{L,R}(\mathbf{r})$ into $g_{L,R}(\mathbf{k})$, and backspace substitute them in real coordinates. This can be done either analytically [24] or iteratively [43]. The gain of such computationally overwhelming approach is that (N, N) \mathcal{G}_{L0} and \mathcal{G}_{R0} matrices can be obtained. From equation (23) we now get:

$$-\tau_L^\dagger g_L \tau_L \mathcal{G}_0 + (EI - H_0) \mathcal{G}_0 - \tau_R^\dagger g_R \tau_R \mathcal{G}_0 = I. \quad (27)$$

If we now define the *self-energies* of the two contacts as

$$\Sigma_L = \tau_L^\dagger g_L \tau_L \quad (28)$$

$$\Sigma_R = \tau_R^\dagger g_R \tau_R, \quad (29)$$

we can obtain the final version of the Green's function matrix of the device that takes also account for the interaction with the two contacts via the two self-energy terms:

$$\mathcal{G} = (EI - H_0 - \Sigma_L - \Sigma_R)^{-1}. \quad (30)$$

Conceptually one can think of $\Sigma_{L,R}$ as matrices that by being added to the bare device Hamiltonian result in an effective Hamiltonian that accounts also for the exact effect of the leads. This concept is very powerful and can be extended to other types of interaction that take place in the device channel during conduction (e.g. electron-phonon interactions [44]), although such extensions result only in approximate descriptions, contrary to the ones obtained for the contacts. At this point, we have fixed a standard procedure for the calculation of Green's function of a two-terminal system, which could be easily expanded for multi-terminal geometries. From here on we can focus on the quantities relevant to transport that can be withdrawn from this function.

3.2 Device and contact spectral functions

Equation (30) allows for a plausible computation of a two-terminal system due to its finite matrix character, even if conceptually the effect of the contacts is that of semi-infinite leads. Here we will define and discuss two quantities that are called the spectral functions A and Γ of the device and the contact respectively. The two relations are defined by the anti-Hermitian part of Green's function and the self-energy's function respectively:

$$A = \imath (\mathcal{G} - \mathcal{G}^\dagger) \quad (31)$$

$$\Gamma = \imath (\Sigma - \Sigma^\dagger). \quad (32)$$

Conventionally only A is usually referred to as the spectral function and is related to the density of states of the system, while the Γ matrix is also called broadening matrix and physically represents the strength with which the contacts are bound to the device.

For the derivation of the relationship between the spectral function and the density of states we need to expand Green's function in an eigenbasis. We start off by considering that the eigenfunctions of the Schrödinger equation form an orthonormal set:

$$\langle \psi_\beta, \psi_\alpha \rangle = \delta_{\beta,\alpha}, \quad (33)$$

where $\delta_{\beta,\alpha}$ is the Kronecker delta. From equation (21) and considering the retarded Green's function by adding an infinitesimal imaginary part to the energy we obtain:

$$\mathcal{G}^R = \sum_\alpha \frac{|\psi_\alpha\rangle \langle \psi_\alpha|}{E + \imath\eta - \epsilon_\alpha}, \quad (34)$$

where η is a very small positive number and ϵ_α is the eigenvalue corresponding to eigenfunction $\psi_\alpha(\mathbf{r})$. From equations (31) and (34) we have:

$$\begin{aligned} A &= \imath \sum_\alpha |\psi_\alpha\rangle \langle \psi_\alpha| \left(\frac{1}{E + \imath\eta - \epsilon_\alpha} - \frac{1}{E - \imath\eta - \epsilon_\alpha} \right) \\ &= \sum_\alpha |\psi_\alpha\rangle \langle \psi_\alpha| \frac{2\eta}{(E - \epsilon_\alpha)^2 + \eta^2}. \end{aligned} \quad (35)$$

Since $\eta \rightarrow 0^+$, by integrating over E with a test function we obtain [42]:

$$A = 2\pi \sum_\alpha \delta(E - \epsilon_\alpha) |\psi_\alpha\rangle \langle \psi_\alpha|. \quad (36)$$

We know that the expression for the Density of States of the system is [29]:

$$D = \sum_\alpha \delta(E - \epsilon_\alpha) |\psi_\alpha|^2. \quad (37)$$

From the last two equations we obtain:

$$2\pi D = \text{Trace}(A). \quad (38)$$

Similarly, the broadening matrix can be also related with the electronic structure of the system. As its name suggests, it gives rise to a broadening of the energy levels in the channel, proportional to the strength of the coupling between the device and the contacts. Furthermore, it introduces a finite lifetime for the electronic states, suggesting that an electron introduced into a state at some point escapes to the contact. References [24,29] propose a detailed mathematical and conceptual derivation of these physical aspects starting from simple toy models all the way up to second quantization arguments. Finally, a useful identity between A and Γ that can be found easily [24] is:

$$A = \mathcal{G}\Gamma\mathcal{G}^\dagger = \mathcal{G}^\dagger\Gamma\mathcal{G}. \quad (39)$$

3.3 Electron density

Next we will discuss the density matrix, whose diagonal elements give the electron density of the device. When contact reservoirs with different electrochemical potentials are attached to the device, each one of them tries to “bring” the device to its own electrochemical potential by injecting or subtracting electrons. If we consider the system in equilibrium (i.e. the device part connected to just one contact), the charge density matrix ρ is given by:

$$\rho = \sum_{\alpha} f_0(\epsilon_{\alpha} - \mu) |\psi_{\alpha}\rangle \langle \psi_{\alpha}|, \quad (40)$$

where μ is the electrochemical potential of the contact and

$$f_0(\epsilon_{\alpha} - \mu) = \frac{1}{1 + e^{\frac{\epsilon_{\alpha} - \mu}{k_B T}}} \quad (41)$$

is the statistical Fermi-Dirac distribution of electrons. Equation (40) can be rewritten within the single-particle scattering theory notation as [29]:

$$\rho = \frac{1}{2\pi} \int_{-\infty}^{\infty} dE f_0(E - \mu) A \quad (42)$$

$$= \frac{1}{2\pi} \int_{-\infty}^{\infty} dE f_0(E - \mu) [\iota(\mathcal{G} - \mathcal{G}^\dagger)] \quad (43)$$

$$= \frac{1}{2\pi} \int_{-\infty}^{\infty} dE f_0(E - \mu) \mathcal{G}\Gamma\mathcal{G}^\dagger. \quad (44)$$

If we generalize now the previous equation for the case of two (and furthermore easily expand for N) contacts we get the final form for the equation of the density matrix:

$$\rho = \frac{1}{2\pi} \int_{-\infty}^{\infty} (f_L \mathcal{G}\Gamma_L \mathcal{G}^\dagger + f_R \mathcal{G}\Gamma_R \mathcal{G}^\dagger) dE, \quad (45)$$

where $f_{L,(R)}$ is the Fermi-Dirac function of the left (right) contact.

3.4 Transmission

The term transmission formalism refers to the theory developed by Imry and Landauer [45] and afterwards

expanded by Büttiker for the calculation of current in nanodevices on the basis of the summation of the *transmission probability* of each *transverse mode* of the device channel [24]. This can be better visualized from the well-known Landauer formula for the conductance:

$$G = \frac{2e^2}{h} MT \quad (46)$$

here G is the conductance, M the number of transverse (or propagating) modes of the device and T the average probability that an electron injected from the one contact will transmit to the other. By defining $T(E) = MT$ as the total transmission probability of the channel for energy E it is straightforward to show [29] that in the case of coherent transport the total current can derive by the relation:

$$I = \frac{2e}{h} \int_{-\infty}^{\infty} T(E) [f_L - f_R] dE. \quad (47)$$

Here the contact Fermi functions represent the driving force for the propagation of current [46] in the sense that only carriers with energies in-between the electrochemical potentials of the two contacts participate in the conduction process. This implies that the usual idea that considers the electric field acting on all electrons as the primary reason for transport is inaccurate. The point is to show how we can relate the transmission and the single-particle scattering formalism.

Under non-equilibrium, we can think of the current that passes from a contact to the device as the difference of an influx and an outflux current [47]. We can write the outflux from the device to the left contact as:

$$I_{out_L} = \frac{e}{h} \int_{-\infty}^{\infty} \text{Trace}(\Gamma_L \rho) dE, \quad (48)$$

and the outflux from the device to the right contact as:

$$I_{out_R} = \frac{e}{h} \int_{-\infty}^{\infty} \text{Trace}(\Gamma_R \rho) dE, \quad (49)$$

where $\frac{\Gamma_{L,(R)}}{h}$ represent the *rate* at which electrons escape from the device to the left (right) contact (considering that Γ matrices have the dimensions of energy) and ρ is the density matrix given by equation (45). Now we can think of the influx current from the contacts to the device as equal to the outflux current we would have if the device was in equilibrium with each one of the contacts:

$$\begin{aligned} I_{in_L} &= \frac{e}{h} \int_{-\infty}^{\infty} \text{Trace}(\Gamma_L \rho_{eq}) dE \\ I_{in_R} &= \frac{e}{h} \int_{-\infty}^{\infty} \text{Trace}(\Gamma_R \rho_{eq}) dE \end{aligned} \quad (50)$$

where

$$\begin{aligned} \rho_{eq} &= \frac{1}{2\pi} \int_{-\infty}^{\infty} (f_L [\mathcal{G}\Gamma_L \mathcal{G}^\dagger + \mathcal{G}\Gamma_R \mathcal{G}^\dagger]) dE \\ &= \frac{1}{2\pi} \int_{-\infty}^{\infty} (f_R [\mathcal{G}\Gamma_L \mathcal{G}^\dagger + \mathcal{G}\Gamma_R \mathcal{G}^\dagger]) dE, \end{aligned} \quad (51)$$

since in equilibrium conditions $\mu_L = \mu_R$. The net current for contact L is:

$$I = I_{in_L} - I_{out_L} = \frac{e}{h} \int_{-\infty}^{\infty} \text{Trace} (\Gamma_L \mathcal{G} \Gamma_R \mathcal{G}^\dagger) (f_L - f_R) dE. \quad (52)$$

With a similar procedure for the second contact we can derive that:

$$I = I_{in_R} - I_{out_R} = \frac{e}{h} \int_{-\infty}^{\infty} \text{Trace} (\Gamma_R \mathcal{G} \Gamma_L \mathcal{G}^\dagger) (f_L - f_R) dE. \quad (53)$$

If we multiply equations (52) and (53) with 2 in order to account for the spin factor and compare them with (47), we can write the transmission probability as:

$$\begin{aligned} T(E) &= \text{Trace} (\Gamma_L \mathcal{G} \Gamma_R \mathcal{G}^\dagger) \\ &= \text{Trace} (\Gamma_R \mathcal{G} \Gamma_L \mathcal{G}^\dagger) \\ &= \text{Trace} (\Gamma_L A_R) \\ &= \text{Trace} (\Gamma_R A_L). \end{aligned} \quad (54)$$

3.5 Electronic Hamiltonians

An important problem that precedes quantum transport is the correct treatment of the electronic structure of the system in study by writing a proper electronic Hamiltonian. In computational codes there are two common approaches to this problem with an accuracy/efficiency mismatch between them, i.e. *ab initio* and semiempirical approaches. *Ab initio* (or *first principles*) methods use only fundamental physical constants and calculate self-consistently the wavefunction of the studied system on the basis of a variational principle of energy minimization. A particular category of *ab initio* methods is the Density Functional Theory, where the fundamental quantity is the electron probability density ρ and not the electronic wavefunction. *Semiempirical* methods on the other hand use simpler Hamiltonians that are parameterized on the basis of experimental data or first-principles calculations. In this case no self-consistent loop is necessary for the calculations, enhancing computational efficiency. However, the static character of such Hamiltonians imposes limitations in their capability to describe systems outside the scope of the initial parameterization. In this sense evaluation or calibration of semiempirical models is necessary prior to their use in electronic structure and quantum transport calculations of a particular system. Here we will see the basic concepts of two methods widely used throughout the this work, i.e. the semiempirical extended Hückel theory (EHT) and the first-principles DFT method.

3.5.1 Extended Hückel theory

The EHT method is one of the most important one-electron molecular orbital semiempirical theories for the calculation of the electronic structure. It is based on the approximation of treating valence electrons separately

from the rest and uses Slater-type atomic orbitals as basis functions for the construction of the Hamiltonian type:

$$f_{nml}^\zeta(r, \theta_1, \theta_2) = N r^{n-1} e^{-\zeta r} Y_l^m(\theta_1, \theta_2), \quad (55)$$

where n, m, l are the principle, azimuthal and magnetic quantum numbers and Y_l^m are the spherical harmonics. The molecular orbitals are then formed as a linear combination of the atomic orbitals f :

$$\phi_i = \sum_j c_j f_j, \quad (56)$$

where coefficients c_i and exponents ζ_i are fitted for the individual basis functions to match bandstructure data [48]. Diagonal Hamiltonian elements are usually calibrated by experimental or first-principles obtained values of the difference between ionization potential and electron affinity:

$$H_{mm} = E_{mm}. \quad (57)$$

For the off diagonal elements the following expression is used:

$$H_{mn} = \frac{1}{2} K (H_{mm} + H_{nn}) S_{mn}, \quad (58)$$

where K is the Wolfsberg-Helmholtz constant (usually having values within 1 and 3) and S_{mn} is the overlap matrix between orbitals ϕ_m and ϕ_n :

$$S_{mn} = \int \phi_m^*(\mathbf{r}) \phi_n(\mathbf{r}) d^3\mathbf{r}. \quad (59)$$

The power of the EHT lies in its good capacity to describe qualitative characteristics of more accurate Hamiltonians with a real-orbital localized basis set that enhances transferability and an overall reduced computational cost.

3.5.2 Density functional theory

DFT is founded on the Hohenberg-Kohn theorems and the Kohn-Sham (KS) formulation that allows for its practical use for the calculation of the electronic structure. The first Hohenberg-Kohn theorem states that the ground state electronic energy E_0 is a unique functional of the ground-state electron probability density ρ_0 , i.e. $E_0 = E_0[\rho_0]$ [49]. Therefore DFT attempts to calculate ground-state properties from ρ_0 . The second Hohenberg-Kohn theorem (also known as the Hohenberg-Kohn variational theorem) states that the exact ground-state electron density minimizes the energy functional $E_0 = E_u[\rho_0]$ [49]. In principle, if we know ρ_0 it is possible to calculate all the ground-state properties from it without having to calculate the wavefunction. However, the Hohenberg-Kohn theorems do not tell us how to calculate E_0 from ρ_0 . The solution to this problem comes with the Kohn-Sham method that translates a problem of n interacting electrons in a noninteracting one by the definition of a fictitious reference system that experiences an external potential $u_s(\mathbf{r}_i)$ that makes the ground-state probability density $\rho_s(\mathbf{r})$ equal to the exact ground-state density $\rho_0(\mathbf{r})$ of the interacting system.

Since the electrons do not interact in the reference system, single-electron orbitals should derive from:

$$\left(-\frac{\hbar^2}{2m}\nabla^2 + u_s(\mathbf{r})\right)\phi_i(\mathbf{r}) = \epsilon_i\phi_i(\mathbf{r}), \quad (60)$$

where the electron density ρ_s is:

$$\rho_s(\mathbf{r}) = \sum_{i=1}^n |\phi_i(\mathbf{r})|^2. \quad (61)$$

Under the Kohn-Sham approach all many-body effects are described by the exchange-correlation potential, defined as:

$$u_{xc}(\mathbf{r}) = \frac{\delta E_{xc}[\rho](\mathbf{r})}{\delta \rho(\mathbf{r})}, \quad (62)$$

where $E_{xc}[\rho]$ is the exchange-correlation energy.

3.6 Nonequilibrium electrostatics

A key characteristic of conduction is that devices are at a nonequilibrium condition due to the separation of the electrochemical potentials of the contacts by the application of bias. Nonequilibrium charging effects are therefore crucial for the correct description of the transport process. The insertion of charging effects in the single-particle scattering theory simply takes places by the addition of a self-consistent potential U_{sc} that is a functional of the electron density to the bare device Hamiltonian [29]:

$$H = H_0 + qU_{sc}, \quad (63)$$

where H_0 is the device Hamiltonian without the presence of electron-electron interactions and q is the electronic charge. The calculation of U_{sc} takes places by numerically solving the Poisson equation:

$$\nabla^2 U_{sc} = -\rho_f/\epsilon, \quad (64)$$

where ρ_f are mobile charges that can be easily calculated within the Green function scattering theory [50] and ϵ is the dielectric constant of the material in which the device part is embedded. Computationally, the calculation of equation (64) takes place within finite difference/elements methodologies in real or momentum space grids using appropriate boundary conditions (usually Neumann and Dirichlet) that account for the different contact configurations (e.g. source, drain or gate electrodes).

3.7 Numerical optimizations

The underlying structure of a computational code is largely based on iterative matrix algebra operations (e.g. matrix diagonalizations and inversions) that scale as $\sim N^3$, where N are matrix dimensions. It becomes evident that computational overloading can easily result for systems of moderate dimensions (e.g. if we consider a graphene nanoribbon with 1000 atoms and describe the electronic

structure within the EHT using a $2s2p^33d^5$ basis we obtain matrices with [9000, 9000] dimensions). To override related difficulties common computational techniques usually fall within two general categories, i.e. optimization algorithms and parallelism.

Most optimization algorithms take advantage of the sparsity in the matrices used within the transport formalism (e.g. Hamiltonian and Green matrices) in order to achieve a reduction in the required operations that goes to a linear scaling of matrix operation with the system size, known as $O(N)$ techniques [51,52]. The underlying algorithms create submatrices with tridiagonal blocks and use the particular properties of the respective matrices to fasten operations. Further optimization can be obtained for particular problems like the calculation of the surface Green matrix [53] that involves costly iterative operations, while energy integrals can be enhanced by division between real and complex contour integration [54]. Finally, use of optimized computational linear algebra libraries (e.g. LAPACK and BLAS) sensibly reduces the processing time.

Parallelism can be achieved at different levels within a quantum transport code. The first level introduces parallelism for the costly matrix operations like diagonalizations and inversions, since the latter occupy the major part of the runtime. A second order scaling can be achieved by the introduction of parallelism for energy integrals, i.e. with the assignment of different energy areas to different processors and linear recombination of the results in the end of each iterative loop. The main drawback of parallelism lies in the need to operate in parallel multicore shared or distributed memory architectures, while the different parallelism protocols (e.g. MPI and OpenMP) give rise to architecture specific codes that lack transferability.

3.8 Summary

In summary, the single-particle scattering formalism can be considered a complete quantum mechanical theory for the calculation of transport in nanodevices that can incorporate a number of scattering mechanisms (contacts, electron-electron, electron-phonon) efficiently. Derivation of all quantities relative to transport can take place with the appropriate definition of the Green matrix, that involves the electronic Hamiltonian written at an appropriate basis set along with information on electron-electron interactions (self-consistent potential U_{sc}), scattering by the contacts (self-energy matrices $\Sigma_{L,R}$) and other scattering mechanisms (self-energy matrices Σ_{ext}). From the Green matrix derivation of the density of states, transmission probability, charge carrier density and current becomes straightforward. The theory can also be extended to calculate conduction for systems where phase-breaking mechanisms are present. On the other hand, criticism to the Landauer-Büttiker approach derives from the intrinsic single-electron picture of the transmission probability that does not take into account for many-body effects, which are enhanced in the nanoscale due to the viscous nature of the electron liquid [55].

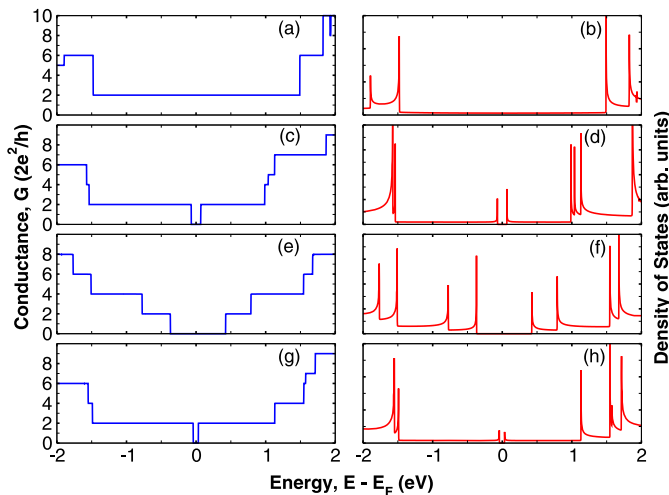


Fig. 9. Ideal conductance (left column) and density of states (right column) as a function of energy for (a, b) a (5, 5) aCNT, (c, d) a (9, 0) zCNT, (e, f) a (6, 8) chiral CNT, and (g, h) a (8, 2) chiral CNT. Results are based on the EHT model.

4 Role of defect scattering

A key aspect of the conduction properties of quasi-1D systems is the presence of quantized steps of conductance (see Fig. 9) that correspond to the 1D subbands of the electronic structure. In fact, the conductance of ideal systems in the ballistic regime can be calculated by a simple summation of the modes that are present in the electronic structure at a given energy (e.g. see Refs. [27,48]), taking into account that each mode carries conductance equal to the conductance quantum $G_0 = 2e^2/h$ [24]. However, structural defects (i.e. vacancies, impurities etc.) can induce perturbations that can strongly influence the transport scenario, giving rise to a deviation of the ideal conductance aspects. This chapter will focus on the problem of defect localization in quasi-1D graphene-based structures. The aim here is to investigate the electronic structure alterations that arise due to the presence of defects and discuss their transport implications, starting from systems with single scatterers all the way up to finite defect concentrations.

4.1 Defect modelling in graphene-based systems

As the simplest paradigm of a non-ideal lattice, vacancies [28,56–60] have an extremely important interest for the general understanding of the various defect scattering mechanisms in graphene-based systems. They can be modelled within the nearest-neighbour TB theory either by a local point potential $\epsilon_i \rightarrow \infty$ that is introduced on the vacancy site, or by the prohibition of overlap interactions from and to the neighbouring sites. This model gives rise to a single semi-localized state with an exact resonance at the Fermi level of the system, while neighboring sites present a C_3 point symmetry and a local magnetic moment [28,58]. This formalism has been widely used for

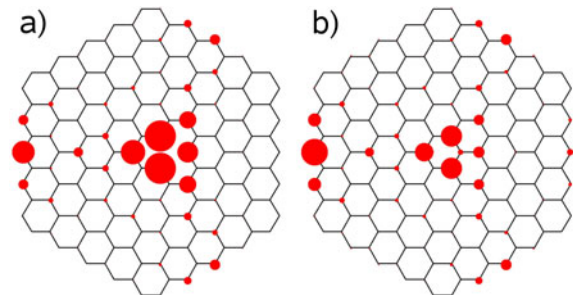


Fig. 10. Schematic representation of the electron probability density $|\Psi^2|$ by means of the TB model for the highest occupied molecular orbital of a hexagonal graphene quantum dot. Two different parametrizations of the vacancy site i are considered, (a) $t_{ij} = 0$ eV within the vacancy and the neighbouring sites j , and (b) $t_{ij} = 1.9$ eV and $\epsilon_i = 10$ eV. The radius of each circle is proportional to the amplitude of the $|\Psi^2|$ value on that atomic site.

quantum transport calculations of defected GNR [61,62] and CNT [63] structures. However, the resonance of this zero-energy mode is highly related to the electron-hole symmetrical description of the bandstructure under the TB model. Only by considering the simplest extension of the TB description to a next-to-neighbor interaction, the valence and conduction band mirror-symmetry breaks and the defect state loses its symmetrical allocation. First-principles calculations have shown that the resonance of this mode is located at energies that are lower than the Fermi level of graphene-based structures [56,64]. Moreover, by breaking of electron-hole symmetry other semi-localized states appear in the eigenspectrum [28], implying that the perturbation is not only constrained to a single energy.

A further analysis of vacancy modelling in graphene-based structures shows that the problem of the resonant energy for the defect states is not the only one. A comparison between the eigenvectors of corresponding defect states in the case of hexagonal graphene quantum dots by means of various ab initio and semiempirical approaches has shown that the nearest-neighbor TB model gives rise to an “approximate” description that can be misleading in the case of quantum transport calculations of defected sp^2 structures [64]. Such implication should impose the use of more sophisticated tight-binding or ab initio models for a correct evaluation of the vacancy-induced perturbations, increasing though the computational load. As a remedy, a further parameterization of the vacancy site has been proposed [64] in order to obtain states around the charge neutrality point which reproduce the correct symmetries of the ab initio calculations (see Fig. 10). The tuned values proposed are $\epsilon_i = 10$ eV for the on-site energy and $t_{ij} = 1.9$ eV for the hopping parameter, with respect to the $\epsilon_i \rightarrow \infty$ and/or the $t_{ij} = 0$ eV of the non-parameterized case. This TB calibration gives also rise to a key conceptual issue, where vacancies behave similarly to p -type impurities (e.g. boron), since the on-site energy lowers from ∞ to a big finite value and the hopping integral raises from 0 eV to finite value [28].

4.2 Scattering from single defects and impurities

The importance of scattering by various types of defects and impurities in the transport properties of sp^2 carbon-systems has been pointed out initially for carbon nanotubes [65]. There it has been observed that the effect of just a single defect/impurity can give rise to conductance reduction equal to a quantum unit. Such a phenomenon would not alter the conductive character of metallic CNTs, since their conductance plateau near the Fermi level (E_F) is equal to two quantum units (i.e. $2G_0$) [30] as a consequence of symmetry-induced subband degeneracy [31]. However, in the case of metallic GNRs the subbands are not degenerate around E_F and the conductance plateau near the Fermi level is equal to G_0 . As a result, resonant backscattering phenomena from defects in GNR structures give rise to conductance pseudogaps [15,16,66,67] that can be fundamental for a bandgap engineering in graphene-based systems and a successive use as active components in microelectronics. The objective here is to discuss the importance of wave function localization induced by defects and impurities for the electrical transport properties of quasi one-dimensional systems and explore the mechanism that gives rise to resonant backscattering phenomena during conduction.

As a starting point for the defect scattering mechanism, we consider a GNR system with a single vacancy, whose presence gives rise to a number of quasi-localized states within the eigenspectrum. These eigenstates have different resonant energies, levels of localization and wave vector composition, while they can give rise to either localized or expanded perturbations in the electronic structure of the ribbons according to their position in the GNR structure, the width of the GNR and the confinement of its edges [16]. The origin of this behavior can be traced back in the electronic structure of the respective ideal system: the shape of the GNR wave functions is confinement-dependent, i.e. it changes for different widths and edge-types giving rise to local alterations of the wave vector's value. When a defect's location coincides with a zero (or extremely small) wave vector value for the respective ideal GNR, the perturbation induced on the electronic structure remains energetically constrained. Contrary, when the defect lies in a GNR region with a finite wave vector value such perturbation expands energetically (see the density of states according to the position of the defects at Fig. 11). The sum of the perturbative behaviors by the defect-induced states is the reason for electron backscattering during conduction. As noticed before, the effect has a particular significance in the conductance plateau around E_F where the scattering gives rise to transport gaps at energies that are related to the resonances of the defect states. The same analysis can be readily extended to other types of in and out-of-plane defects, impurities or adsorbates in GNRs [66–68] or CNTs [69], with a principal differentiation: each defect-type can give rise to localized states with distinct resonances that correspond to dips at different energies in the conductance spectrum. This last feature can be fundamental for the tuning of CNT/GNR transport properties on the basis of a controlled structural

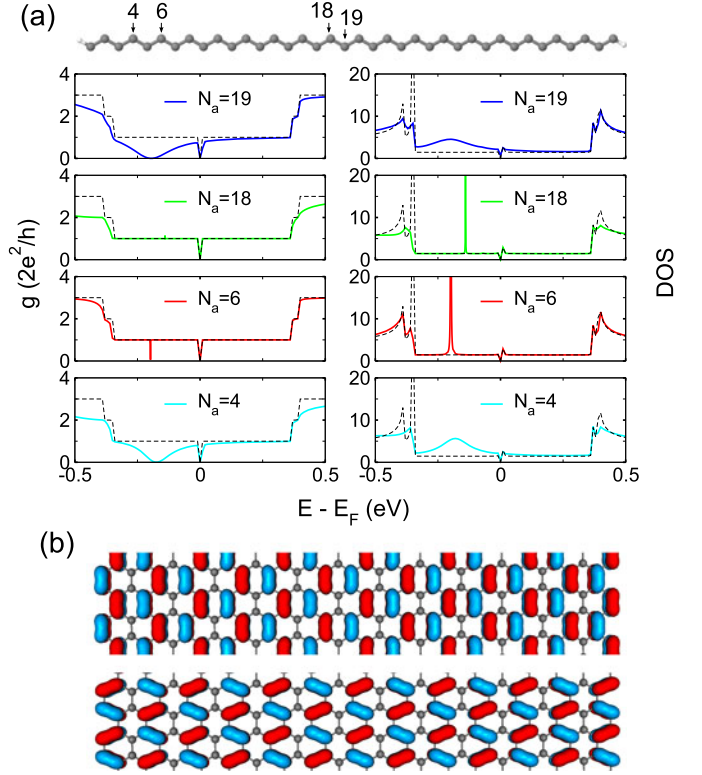


Fig. 11. (a) Conductance g and DOS as a function of energy for a 38-aGNR with single vacancies at different positions N_a . Dashed lines show values for the respective ideal structure. (b) Projection of the wave function corresponding to first state below the charge neutrality level (upper) and the first state above the charge neutrality level (lower) for a non-defected 38-aGNR.

or chemical functionalization. The role of extended defects (e.g. divacancies, grain boundaries, etc.) in confined graphene systems has not yet been thoroughly studied. However, previous considerations should be valid also in this case, noting that due to the spatial expansion of these defects that usually exceeds the wave function lateral quasi-periodicity of the respective ideal systems, backscattering effects should always be present.

A reasonable question here is if and when we can quantify the backscattering mechanism for various GNR and CNT structures. The answer is simple only in the case of GNRs with armchair edges, where an analytic expression can be obtained for the wave functions of the ideal systems [34]. In the case of metallic aGNRs it is easy to construct a simple rule: for $N_a = 3p + 2$ dimer lines ($\forall p \in \mathbb{N}$), defects at the $N_a = 3q$ sites do not affect the first conductance plateau ($\forall q \in \mathbb{N}, \leq p$), while the rest give rise to conductance pseudogaps at energies that correspond to the defect resonances. In the case of GNRs with zigzag edges, the absence of a purely analytical formula for the derivation of the wave functions makes necessary a computational approach for the verification of backscattering issues from defects. Here, for both vacancies [16] and impurities [66,70] can give rise to transport gaps with both donor and acceptor characteristics (Fig. 12). It is moreover

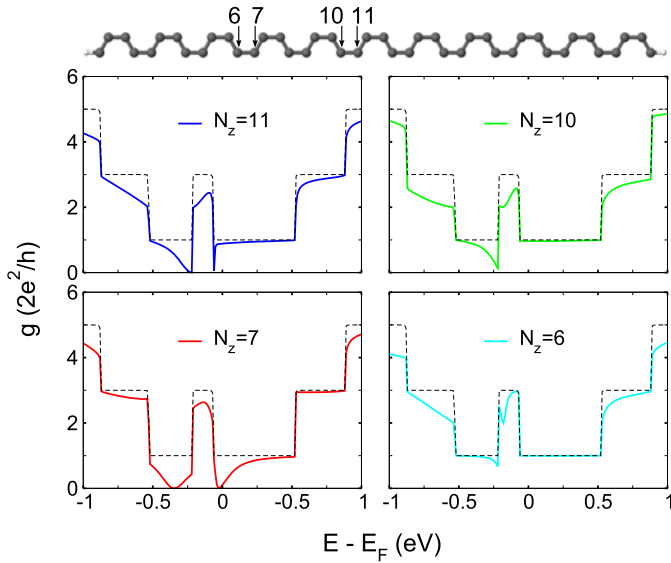


Fig. 12. (a) Conductance g as a function of energy for a 22-zGNR with a single vacancy at the $N_z = 11$ (up-left), $N_z = 10$ (up-right), $N_z = 7$ (down-left) and $N_z = 6$ (down-right) positions.

important to notice that the zigzag-edge confinement enhances the role of the positioning of the various defects along the width of the structure, where backscattering effects within the entire conductance plateau can be obtained [71]. This is due to the presence of a high density of states within this plateau, where different wave vectors can be perturbed according to the resonance of the defect states. In the case of CNTs the periodic boundary conditions of the structure (i.e. the rolling of the graphene sheet) do not impose any differences between the various sites of the atoms within the unit cell and therefore the backscattering mechanism should be independent of the position of the defect/impurity for a given CNT. Differentiations in the dip resonances are expected though for different CNTs and different types of defects [65].

Finally, defects in sp^2 carbon structures can be related to interesting non-equilibrium electrostatic phenomena within the conduction process. It has been shown through a self-consistent Schrödinger-Poisson methodology that vacancies can behave as local charging centers that can induce electrostatic inhomogeneities on the GNR topology [16]. The magnitude of this effect is bias-dependent, i.e. by increasing the electrode bias a more intense electrostatic inhomogeneity pattern has been calculated. This picture can be directly related to experimental measurements of the conductance in graphene sheets with local impurities [72].

4.3 Scattering from finite defect/impurity concentrations

An extrapolation of the results discussed in the previous section indicates that the electronic transport behavior of quasi-1D carbon systems could be strongly sensible to the

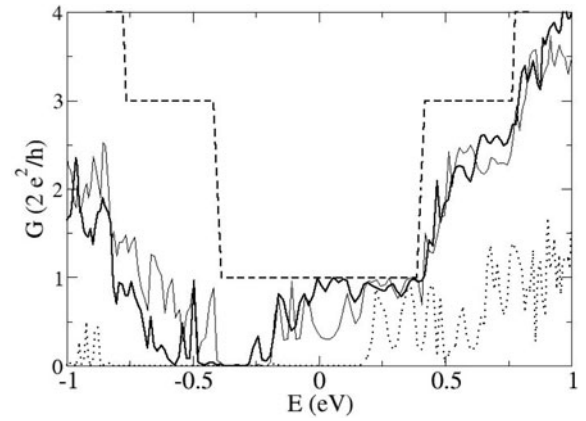


Fig. 13. Conductance spectra of a 35 aGNR with length $L = 43$ nm with different random distributions of boron impurities: 1.4‰ density in bulk or edge positions (thick solid line), 1.4‰ density in edge only positions (thin solid line) 1.4% in bulk or edge positions of the GNR (dotted line). The conductance of a pure GNR is also shown as a reference (dashed line).

inclusion of a finite density of defects or impurities. In the low density limit we can assume that the local alterations due to the defects on the system Hamiltonian can be independently mapped by using single defect calculations. This procedure allows to accurately evaluate the conductance of relatively large defective systems ($\sim \mu\text{m}$). In Figure 13 we show the conductance of p -doped (due to boron inclusion) GNRs in the case of three different space distributions of the scattering centers at a fixed density. The alterations of the conductance are more significant at the resonant energies; however fluctuating values of G are calculated in the whole spectrum and the hole-electron symmetry is, in general, broken. Similar features can be recovered for the CNT case [73]. As we can expect $G(E)$ significantly changes with the disorder realization even when we fix the system's size and the density of scattering centers. As a consequence, in order to correlate systematically the conductance features to the average disorder status, a statistical analysis is needed using a large number of equivalent replicas of the same system.

Coherent electron transport in a 1D system is characterized by the localization phenomenon firstly stated in the Anderson's seminal paper of reference [74]. The multiple interference due to random distributed scattering centers should lead to an exponential increase of the 1D conductor resistance $r(E) = 1/g(E)$ with its length L

$$\langle \ln r(E) \rangle = 2L/\xi(E) + c. \quad (65)$$

The average resistance is then ruled by an energy dependent single parameter $\xi(E)$, called localization length, uniquely related to the disorder realization. Numerical analyses have established that quasi-1D carbon nano-systems are in the localization regime also for a relatively low concentration of impurities or defects of the order of 0.1% [15,67,74]. In particular, the exponential dependence is strong (i.e the localization length is of the order

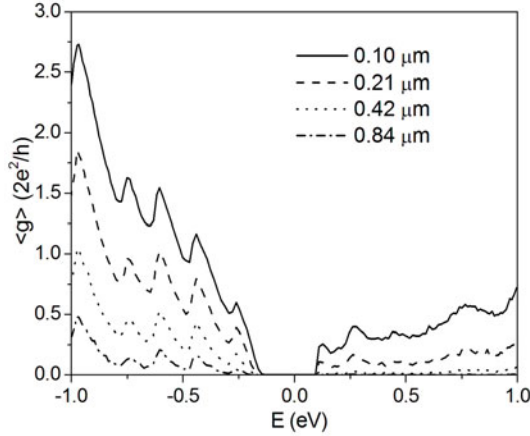


Fig. 14. Average conductance $\langle g \rangle$ as a function of the energy E , for an N-doped $N = 45$ aGNR of different lengths. Plotted values represent statistical averages over more than 500 equivalent replicas of the system. Charge neutrality points of pure and doped systems are aligned at $E = 0$ in the figure.

of 10 nms and below) in the energy region of the resonance states.

In Figure 14 we show the (small bias) average conductance of an ideally contacted 45-aGNR doped with a 0.2% density of nitrogen atoms and for systems with increasing length L , from $0.1 \mu\text{m}$ to $0.8 \mu\text{m}$. An asymmetric decrease of the average conductance due to the impurity scattering can be observed in the whole spectrum. This behavior is particularly important in the energy region near the single impurity resonance states (i.e. for energies ~ 0.2 eV) where a mobility gap (i.e. a region with almost null conductance but with a huge density of states) appears also for the smaller systems. We note that the ideal 45-aGNR is a semiconductor GNR with a energy gap ~ 0.2 eV.

A qualitatively similar behavior has been calculated for doped GNRs if the reference ideal system is either metallic or semiconducting. Equivalent conductance features can be found in an N-doped 45-aGNR and 47-aGNR (compare e.g. Figs. 14 and 15). In the latter case the ideal system has a quasi-metallic behavior with the first plateau of the conductance extending for ~ 0.5 eV around $E = 0$.

In the vacancy-damaged (V-damaged) case a large mobility gap appears in the negative energies region (hole band) due to the strong backscattering of the defects (Fig. 15 dotted line). However, apart from the intensity of the scattering, V-defected GNR manifest the behavior of a system doped with p -type impurities in the localization regime.

From an analysis of the conduction spectra we can derive some general features which can be useful for the interpretation of electrical characterization in real GNRs. Indeed, we note that the conduction spectrum can be measured in a three terminal configuration [75] tuning the gate potential in order to modify the electron density in the nanostructure. Firstly, we note the persistence of the conduction modulation with energy in disordered systems, related to the correspondent conductance plateaus of the subband structure in ideal GNRs. Moreover, the effective

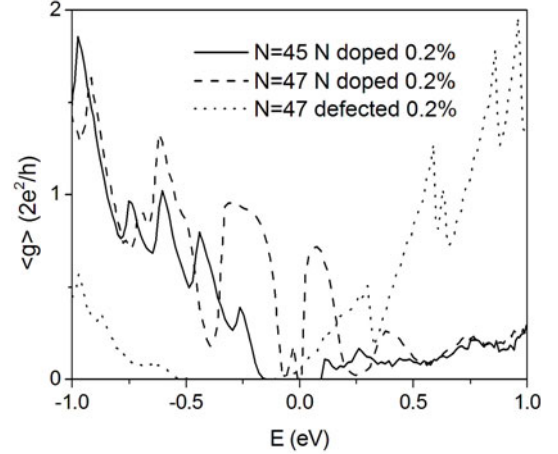


Fig. 15. Average conductance $\langle g \rangle$ as a function of the energy E , for N-doped $N = 45$ aGNR (solid line), N-doped $N = 47$ aGNR (dashed line) and V-damaged $N = 47$ aGNR (points) with fixed length: $L \sim 0.21 \mu\text{m}$. Plotted values represent statistical averages over more of 500 equivalent replicas of the system. Charge neutrality points of pure and defected systems are aligned at $E = 0$ in the figure.

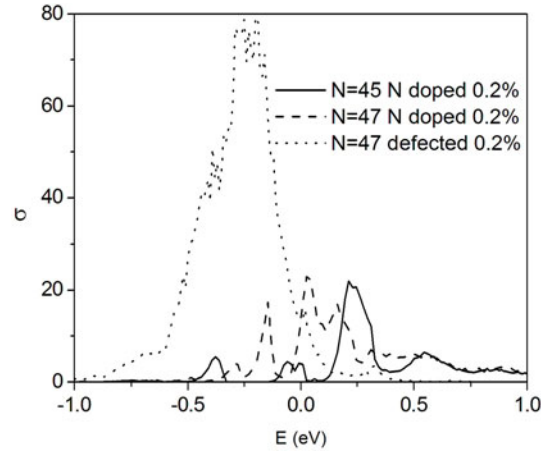


Fig. 16. Conductance fluctuation σ as a function of the energy E , for N-doped $N = 45$ aGNR (solid line), N-doped $N = 47$ aGNR (dashed line) and V-damaged $N = 47$ aGNR (points) with fixed length: $L \sim 0.21 \mu\text{m}$. Plotted values represent statistical averages over more of 500 equivalent replicas of the system. Charge neutrality points of pure and defected systems are aligned at $E = 0$ in the figure.

transmission in the subbands is strongly reduced due to the localization effects with a more significant suppression of the transparency in the energy region where resonance states are located. Finally, the general occurrence of a mobility gap can be hardly distinguished by the gap due to the geometrical confinement in semiconductor GNRs, if conductance measurements are not accompanied by density of states measurements. A distinguished signature of the mobility gap, due to its backscattering origin, is the correspondent huge value of the conductance fluctuations

$$\sigma^2 = \langle \ln(g)^2 \rangle - \langle \ln(g) \rangle^2. \quad (66)$$

In order to demonstrate this statement we have plotted in Figure 16 the statistically evaluated conductance variance for the same cases of Figure 16: in the quasi-metallic systems the conduction depletions are systematically linked to a variance peaks, while the variance in the standard gap of the semiconductor GNRs does not show particular features.

5 Role of contact bonding

A key issue for the integration of quasi 1D carbon systems in devices is their interaction with the metallic electrodes. By itself the concept of low-dimensionality enhances the role of the contact with respect to traditional devices, since electrons have to transmit from a big number of modes present in the metallic electrode to the small number present in the channel material, before exiting again towards the second electrode [24]. Hence, considering coherent regimes, a great part of the scattering mechanisms should derive from the interaction between the channel material and the metallic contacts. The aspects of this interaction can be multiple: equilibrium and non-equilibrium electrostatics, chemical bonding issues and geometrical reconstructions. In this paragraph we will try to briefly discuss these issues for CNT and GNR structures.

5.1 Electrostatic considerations

A first attempt to evaluate the transport properties of carbon nanotubes in contact with a material of a different work function was through the study of CNT junctions [76,77]. From these studies an important electrostatic aspect that characterizes 1D systems came to light, i.e. a long-range Coulomb interaction that gives rise to very long depletion tails in the charge distribution. Such feature can fundamentally modify the charging interactions with respect to conventional semiconductor heterostructures. The equilibrium electrostatic scenario in the case of a metal-CNT junction also provides for the existence of typical band bending phenomena due to work function differences that can give rise to conductance asymmetries in an otherwise quasi-symmetrical spectrum around the Fermi level [77–79]. A further electrostatic aspect at non-equilibrium conditions recognises the difference in the potential screening on the basis of the CNT diameter [80] and the conductive character of the CNT/GNR [81,82]. In both cases the presence of a higher density of states in the carbon structure gives rise to a faster screening near the contact. However, the description of a metal-CNT or similarly a metal-GNR junction on the basis of purely electrostatic criteria misses some important information on the aspects of a realistic reconstruction of a metallic electrode: (a) the coupling between the metal and the carbon atoms, and (b) the role of the geometrical and topological characteristics of the junction.

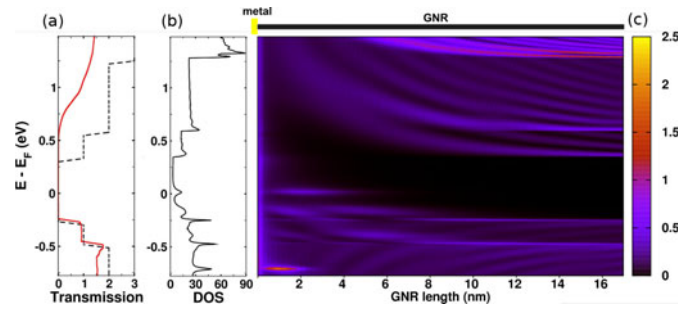


Fig. 17. (a) Transmission coefficient, (b) total density of states and (c) real-space band formation along the GNR length for a semiconducting 16aGNR contacted with Au. Dashed lines represent the transmission coefficient of the respective ideally contacted aGNR.

5.2 A combined electrostatic/chemical picture

In order to address the combined chemical/electrostatic problem here we discuss the low-bias transport properties of a junction between a semiconducting GNR and a gold electrode, as seen in Figure 17. Simulations are based on an atomistic Schrödinger/Poisson scheme that addresses the effects of charging as well as bonding interactions [82]. As a first response to the difference between the work functions ϕ of the electrode and the GNR ($\phi_{Au} > \phi_{GNR}$ in this case), upwards band-bending phenomena can be observed near the metal-aGNR interface. Band-bending is not uniform though for the conduction and the valence bands. The reason can be traced in a quantum interference mechanism where wavelike patterns appear in the band formation of the junction (Fig. 17c) due to the reflection of the incident electron wave by the non-ideal contact [83]. Such patterns shift upward for the conduction band and downward for the valence band, and respond differently in the presence of the electrostatic field induced by the interface charging. For the conduction band, both the electrostatic field and the interference pattern have a similar upward direction. Hence, the whole band bends smoothly giving rise to a state-free zone near the interface. For the valence band instead the apparent opposite directions of the electrostatic field and the interference pattern give rise to local minima and maxima in the band scheme that become discrete localized states inside the bandgap (see Fig. 17c). In addition, metal-induced gap states, i.e. tails of the wave functions of the metallic contact that decay in the semiconducting gap, form throughout the interface. Moreover, the Fermi level of the combined system, although still within the bandgap, loses the midgap position of the ideal (non-contacted) aGNR and moves toward the valence band. The influence of all these features for the conduction mechanism are seen with the calculation of the transmission coefficient for the heterosystem in comparison with that of the ideal system (Fig. 17a). From this picture a low Schottky barrier with respect to the valence band emerges (of the order of 0.2 eV for this heterosystem). Consequently, the distance between the Fermi level and the conduction band increases. Moreover, the conduction band charge flow is strongly suppressed, giving rise to

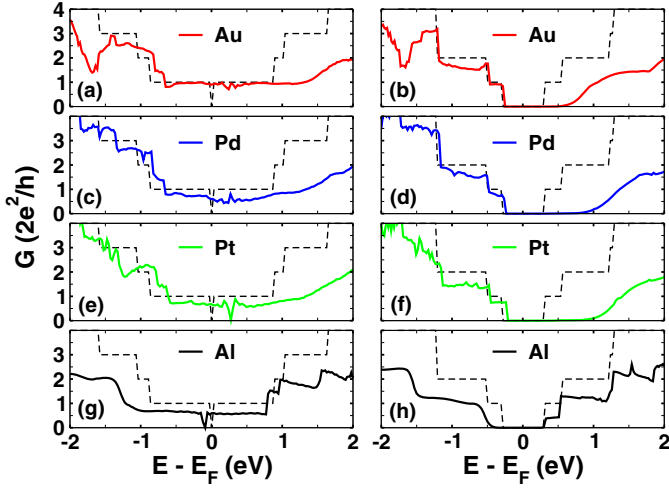


Fig. 18. Conductance as a function of energy for a $N_a = 14$ aGNR (left column) and a $N_a = 16$ aGNR (right column) contacted with: (a, b) Au, (c, d) Pd, (e, f) Pt, (g, h) Al. Dashed lines show ideal conductances for the respective aGNRs.

a selective loss of the conductance quantization information that is typical of the 1D subbands in GNR structures. This behavior is related with the state-free zone near the interface as discussed previously. The combination of Fermi level shifting toward the valence band and the conductance suppression due to band-bending is the reason for the asymmetric form of conductance distribution.

A similar picture arises when the work function of the metal is lower than that of the GNR, with the only difference that the bands now bend downward whereas the Fermi level shifts toward the conduction band. This shift is even more important when the junction is comprised of a metal and a metallic GNR (or CNT). In this case, in addition to the electrostatic and the chemical aspects of the heterostructure, important doping features arise (p -type when $\phi_{metal} > \phi_{GNR}$ and n -type when $\phi_{metal} < \phi_{GNR}$). Effective doping therefore is a fundamental aspect of metal contacted GNRs/CNTs that finds also experimental verification [84,85].

Bonding between the metallic contact and the carbon structure acts complementary to the electrostatic features. Figure 18 shows the influence of chemical bonding in the conduction characteristics of a metallic (14 aGNR) and a semiconducting (16 aGNR) ribbon contacted with Au, Pd, Pt and Al electrodes, within self-consistent atomistic EHT calculations. Higher work function metals with respect to the GNR (i.e. Au, Pd and Pt) give rise to qualitatively similar transport characteristics that originate from the electrostatic aspect of the heterojunctions, as discussed earlier. However, only Au seems transparent near the Fermi level with the conductance arriving at the $1G_0$ plateau of the ideal case, whereas Pd and Pt are slightly less transparent for this energy zone. On the other hand, for the valence band, transparency above the first conductance plateau is improved for Pd and Pt, which show a smaller extent of conductance fluctuations with respect to Au. A pronounced case of the importance of inter-

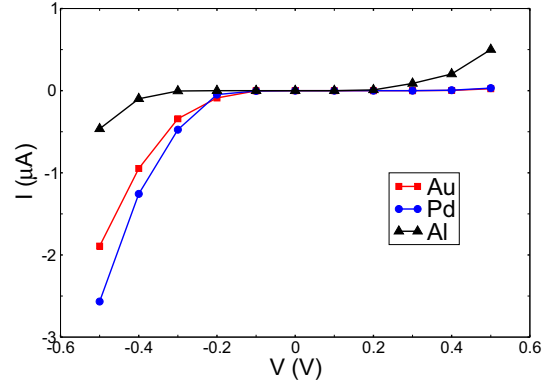


Fig. 19. Non-equilibrium current-voltage characteristics for a $N_a = 16$ aGNR contacted with Au, Pd and Al for drain-to-source biases $V_{DS} = 0-1$ V.

face chemical coupling though is that of the low work function Al electrode (Figs. 18g, 18h). Here, despite the contact-induced n -type doping (for the 14 aGNR) and the ambipolar Schottky behaviour (for the 16 aGNR), the dominant aspect that characterizes conduction is the strong scattering by the contacts. Indeed, in the Al-GNR system contact resistance constitutes the main factor of conductance suppression with respect to the ideal case, with half-blocked conduction channels and overall conductance degradation throughout the energy spectrum. The previous discussion is supported by the current-voltage characteristics of the metal – 16 aGNR junction (Fig. 19). Typical Schottky-diode characteristics are obtained with the high work function Au and Pd electrodes. Larger current values obtained for a negative bias in the case of Pd with respect Au are due to its slighter more pronounced p -type character. Al instead does not reproduce diode-like characteristics whilst on-off current ratios are too small for device operation.

5.3 Geometrical considerations

Another important aspect of the metal-carbon interaction are the geometrical characteristics of the junctions. These can be widely defined by the equilibrium relaxation of the carbon atoms in the case of contacts that are deposited on the CNT or the GNR structure and vice-versa (i.e. the side-contact scheme [86]). However, serious considerations have been raised for the efficacy of side-contacts in terms of chemical bonding with sp^2 carbon allotropes (e.g. due to an insufficient bonding between the two parts of the heterostructure [87]), whereas end-contacts could ideally resolve these issues [88]. Moreover, there are examples of transport measurements where the contact is a microscope tip that simply “touches” the ends of the nanostructure [89]. In this case the role of the geometrical reconstruction of the interface becomes crucial for the transport properties of the system. A simple example can be considered with metallic tips that approach the open end of a CNT structure (see Fig. 20a). Here, by increasing the tip-CNT distance by only a few Å important

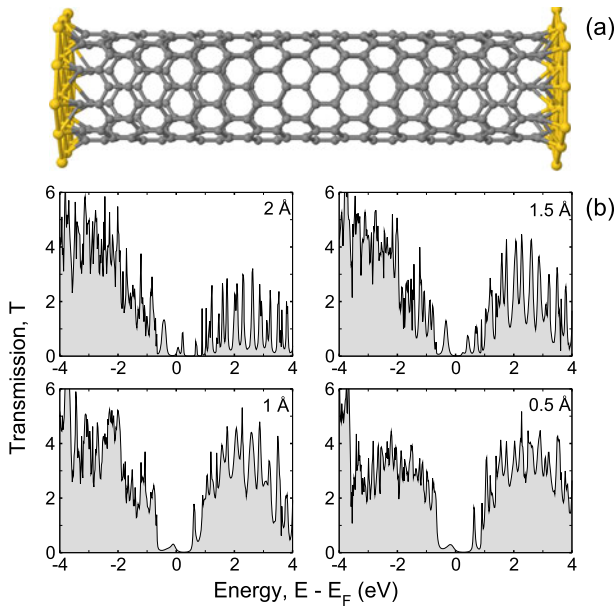


Fig. 20. (a) An 8-unit-cell long (10, 0) CNT end-contacted with Au(111) metallic electrodes. (b) Transmission as a function of energy for four snapshots of a (10, 0) 8-unit-cell system with a varying contact-tube distance of 2 Å, 1.5 Å, 1 Å and 0.5 Å.

alterations in the conductance features can be observed, by means of an overall reduction of the transmission coefficient. Moreover the placement of the metallic tip at a position that does not guarantee the full saturation of the interface carbon bonds can lead to the introduction of dangling bond states at the vicinity of the Fermi level that in the case of short tubes can even become conductive (see Fig. 20a for a 2 Å distance). On the other hand, once a strong interface coupling between the metal and the carbon structure has been achieved, small atom dislocations and interface disorder are not expected to significantly alter the transport features [30].

5.4 Non-equilibrium charging

Apart from the equilibrium aspects of electron charging in metal-CNT/GNR heterostructures (e.g. Schottky-type barriers), electron-electron interactions are also present under non-equilibrium conditions due to the application of bias in the source and drain electrodes. Ideally, in this case the non-equilibrium electrostatics could be defined by a simple Laplace potential term with boundary conditions that are defined by the applied bias. However, this picture ignores the role of the accumulation of charges (both on the device and on the electrode part of the heterojunction). In this case a correct treatment of the non-equilibrium electrostatics in these systems requires the integration of Laplace, Poisson and Image terms in the description of the dynamic electron-electron picture [90–92]. Accounting for these aspects can have an important repercussion in the current-voltage characteristics when the device works in the high-bias regime (e.g.

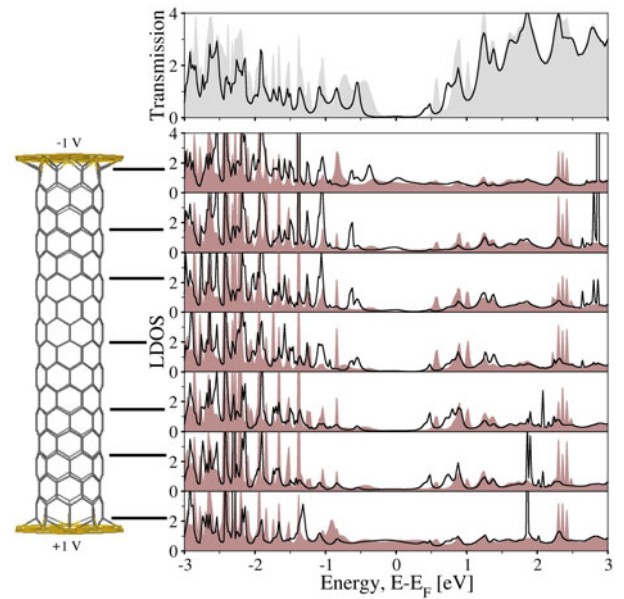


Fig. 21. Geometry, transmission coefficient, and local density of states evaluation as a function of energy and position along the CNT axis for a (8, 0) zCNT contacted with Au. The applied biases are 0 V (shaded area) and 2 V (black line).

$V_{DS} \sim 3$ V). It has been calculated that for CNT [91,92] or GNR [93] structures the current-carrying capacity can be significantly reduced due to the accumulation of charges at the interface that gives rise to a tracking relationship between the electrochemical potentials of the contacts and the local density of states of the device (see Fig. 21). Enhanced charging at high-bias regimes should act in conjunction with the intrinsic resistance of the metal-carbon junction, further reducing the probability of electron transmittance in these systems.

6 Polaronic transport in carbon chains

As we have discussed in Section 2, the electronic structure of carbon chains is strongly interconnected to the deformation status: dimerized chains have a semiconductor (insulator) character while undimerized chains are metallic. The stability of one atomic configuration with respect to the other results in a completely different electrical behavior for the same system. This aspect belongs to a more general issue: i.e. the modification of the bare electronic properties (e.g. effective mass, energy bands) due to the electron-phonon interaction or, more concisely, the polaronic effects.

Whilst the seminal investigations on the polaronic effects are contemporary with the birth of the modern solid state physics [94], the study of the polaronic effects in the electronic transport for nano or molecular systems is a new and intriguing research field. This field has been also stimulated by a series of experiments which have demonstrated, in a wide class of structures, that molecular devices could manifest non-linear transport behavior (e.g.

negative differential resistance (NDR) or switching) also caused by atomic configuration changes [95,96].

A theory (still under development) for the complete understanding of anomalous phonon driven electron dynamics should be based on the non-perturbative (e.g. variational) study of coupling between local vibrations and electrons [97]. In this sense the phonon scattering is not responsible for the diffusive transport, but it rules the distribution in energy of the electronic levels responsible for the conduction in the device. As a consequence, a polaronic transport theory is again related to the coherent electron transport topic and can be properly formulated extending the single-particle scattering method. As it will be clear, the method is consistent with Landauer's approach to the electronic transport and, of course, it relies on the same general framework.

6.1 The non-equilibrium polaronic theory

In the polaron theory, the system Hamiltonian including electron-phonon coupling is approximated using a suitable ansatz for the phonon quantum variables. In general the procedure results in the reduction of the original Hamiltonian to an effective pure electron one $H\{u_i\}$ where the effects of the phonon quantum variables are taken into account by means of a given set $\{u_i\}$ of variational variables. This procedure is rather simple in the adiabatic approximation where the set $\{u_i\}$ practically coincides with nuclear (quasi classical) coordinates (see e.g. Sect. 2); whilst the theory requires a complex ansatz (i.e. additional variational variables) away from the adiabatic limit [95].

If we can neglect electron-electron interactions, or if we can approximate them applying a single particle mean-field scheme, we can formulate the equilibrium polaronic theory, for a system in contact with a particle's reservoir at temperature T and chemical potential μ , on the basis of the free energy functional [98]

$$\Omega_\mu\{u_i\} = -kT \int \ln [1 + \exp(\mu - \epsilon/kT)] n(\epsilon, \{u_i\}) d\epsilon + U_\Omega\{u_i\} + \mu N_0 \quad (67)$$

here N_0 is the total number of electrons ruled by μ , $n(\epsilon, \{u_i\})$ is the density of states at the energy ϵ and $U_\Omega\{u_i\}$ an eventual term independent on the electron occupancy. The best variation estimate of $\{u_i\}$ can be obtained solving the electron problem consistently with the extreme conditions $\delta\Omega_\mu\{u_i\}/\delta\{u_i\}$, which give the stable and metastable equilibrium states of the system.

Extensions of the variational equation to the non-equilibrium case have been proposed [96] and applied to the electron transport based on the concept of electron occupancy in non-equilibrium conditions. These extensions have not a general validity since the variational equations can be explicitly formulated in terms of the electron occupancy only in particular cases. A more general approach

can be obtained by means of a direct numerical minimization procedure based on an extension of the Mermin's functional (Eq. (67)). In the non-equilibrium case, the system is in contact with two leads (i.e. with two independent particle reservoirs) at chemical potentials μ_L and μ_R . According to Landauer's scheme of the electron transport in the stationary coherent case (see Ref. [24]), the device states are populated by electrons ($+k$ states) with an energy distribution $n_L(\epsilon, \{u_i\}) = \text{Tr}(\mathcal{G}\Gamma_L\mathcal{G}^\dagger)/2\pi$ at equilibrium with the left contact and by electrons ($-k$ states) with an energy distribution $n_R(\epsilon, \{u_i\}) = \text{Tr}(\mathcal{G}\Gamma_R\mathcal{G}^\dagger)/2\pi$ at equilibrium with the right contact. In this scheme, following the Gibbs prescription, we could assume that μ_L and μ_R are the natural variables to allow for charge fluctuation in the device for $+k$ and $-k$ states respectively. The same interpretation is given for the chemical potential μ in the equilibrium case when the system is in contact with a single particle reservoir. As a consequence the (quasi) free energy functional for the $+k$ ($-k$) electron states should have a Mermin like expression ruled by the lead chemical potentials

$$\Omega_{\mu_L, \mu_R}\{u_i\} = U_\Omega\{u_i\} + \mu_L N_L + \mu_R N_R - kT \int \ln [1 + \exp(\mu_L - \epsilon/kT)] n_L(\epsilon, \{u_i\}) d\epsilon - kT \int \ln [1 + \exp(\mu_R - \epsilon/kT)] n_R(\epsilon, \{u_i\}) d\epsilon \quad (68)$$

where for symmetry considerations $\mu_L N_L = \mu_R N_R = N_0/2$. Note that, considering the identity $\mathcal{G}(\Gamma_L + \Gamma_R)\mathcal{G}^\dagger = i(\mathcal{G} - \mathcal{G}^\dagger)$, the functional of equation (68) reduces to equation (67) when $\mu_L = \mu_R = \mu$. In the coherent stationary case the current can be calculated by means of the Landauer expression

$$I = \frac{2e}{h} \int_{-\infty}^{\infty} T(\epsilon, \{u_i\}) (f_L - f_R) d\epsilon \quad (69)$$

where the transmission is formally similar to equation (47).

6.2 Insulator-metal transition in biased carbon chains

The variational method introduced in the previous paragraph can be applied to investigate the transport behavior of carbon chain based two terminal devices. The system consists in a chain of N carbon atoms coupled by means of the first ($n = 1$) and last ($n = N$) atoms to two semi-infinite metallic leads. We can assume that a reliable model for this system is the extension of the Hamiltonian equation (18) including the contacts and the device contact coupling

$$H[u_n] + \sum_{k \in \{L, R\}, \sigma} \epsilon(k) c_{k, \sigma}^\dagger c_{k, \sigma} + \sum_{k \in \{L\}, \sigma} V_k c_{k, \sigma}^\dagger c_{1, l, \sigma} + h.c. + \sum_{k \in \{R\}, \sigma} V_k c_{k, \sigma}^\dagger c_{N, l, \sigma} + h.c. \quad (70)$$

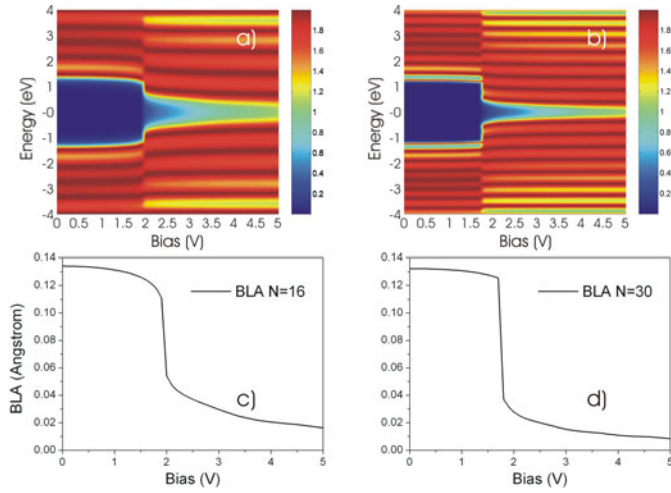


Fig. 22. Transmission (color scale in G_0 units) as a function of the applied voltage V and energy E for $N = 16$ (a) and $N = 30$ (b) carbon chains contacted with $\langle 111 \rangle$ gold leads. (c, d) BLA as a function of V for the same systems.

where k runs over the band states of the left (L) and right (R) contacts and V_k are the device-leads coupling parameters.

In Figures 22a, 22b the calculated transmission $T(E, V)$ as a function of the applied bias V and the energy E is shown for the $N = 16$ and $N = 30$ systems respectively, contacted with a $\langle 111 \rangle$ gold leads. At zero voltage the transmission is practically zero in the gap region while it is characterized by a sequence of peaks reaching a value $\sim 2G_0$ for energy larger (smaller) than the LUMO (HOMO) level. The dimerization gap $\Delta(N = 16) = 2.75$ eV, $\Delta(N = 30) = 2.42$ eV is almost identical to the equilibrium one also at low bias. In the $V = 1.7$ – 1.9 V region the gap value shows a discontinuous decrease and it gradually disappears for larger biases where the system has a metallic-like transmission. The gap reduction is consistently related to a BLA reduction (i.e. to a polyyne-cumulene transition) and Δ progressively tends to zero for large V (Figs. 22c, 22d).

The non equilibrium variational model predicts current voltage characteristics for the C chains systems showing an insulator-metal like transition. This feature is evident in Figure 23 where the calculated I - V curves (solid lines) for the $N = 16$ (Fig. 23a) and $N = 30$ (Fig. 23b) systems are shown. Note that, as we could expect, a classical diode-like characteristic is derived when the transmission is calculated using the equilibrium estimate for the variational variables (dashed lines in Fig. 23).

The predicted behavior of the C chain under bias is related to a configuration change due to non-equilibrium charging which could more generally emerge in a molecular device when the atomic configuration of the molecule is consistently related to a given electron distribution in the molecular orbitals. In the case of a carbon chain the biasing competes with the mechanism on the basis of the Peierls instability: the non-equilibrium electron charging of the chain makes the dimerized state progressively less

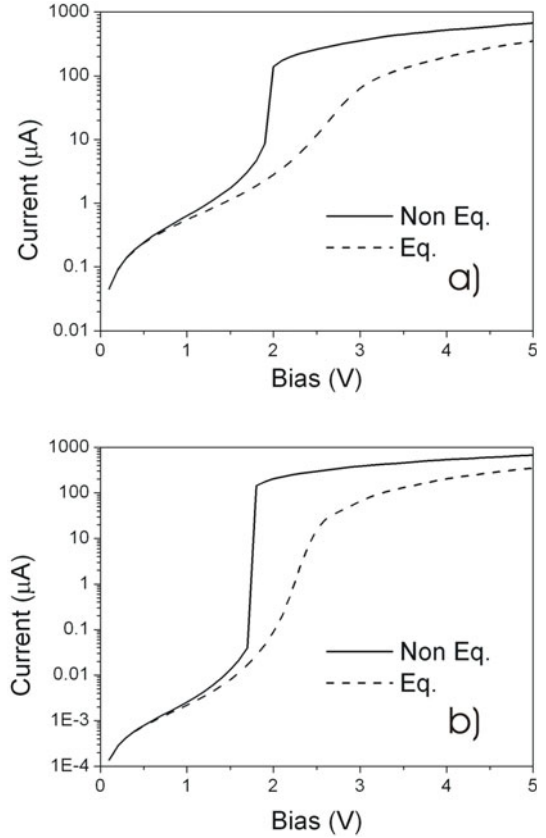


Fig. 23. Self-consistently calculated current voltage characteristic (solid-line) for carbon chains with $N = 16$ (a) and $N = 30$ (b) atoms contacted with $\langle 111 \rangle$ gold leads. I - V characteristics calculated without self-consistency are also shown (dashes).

favoured until both BLA and the gap are strongly reduced. These anomalous non-equilibrium effects could be easily verified in C chain based devices.

This variational method can be extended also to the phonon-variables and it can be easily applied in any calculation based on the Born-Oppenahimer (BO) approximation (e.g. DFT). Considering these results, the estimate of transport characteristics could be crucially modified including this correction. Moreover, the method could be also applied away from the BO limit [7] since it is not limited to the typology of the variational variables. In this sense also the inclusion of the electron-electron interactions in the method could be also of interest since a gap closing mechanism has been recently reported due to pure electron correlation [19].

7 Discussion

As a vastly expanding field, the use of carbon ribbons, tubes or chains in nano-electronics presents a series of advantages with respect to the current semiconductor technology: intrinsic low-dimensionality, mechanical stability and elasticity, exceptional electrical, optical and thermal properties to name but a few. On the other hand, the same extreme manifestation of low-dimensionality (i.e. an

one-atom-thickness) implies that the potential device integration of these materials is subject to understanding and controlling both internal and external sources of perturbation. In this Colloquium we have discussed how various sources of non-ideality in these materials can influence their conduction characteristics. Defects and impurities can give rise to transport gaps, and in higher concentrations, to strong conductance fluctuations and an overall suppression of the electron transmission. Metallic contacts can act as important scattering and doping centers that can induce conductance asymmetries and electrostatic barriers. Finally, by itself the application of bias can give rise to non-equilibrium resistive phenomena and in the particular case of carbon chains also to metal-insulator transitions.

A further theoretical investigation on the sources of non-ideality in sp^2 carbon-based devices should take place in the future, since experimental evidence indicates that disorder and environmental interactions are the most important factors that hinder the ideal transmission of electrons in these systems. Toward this direction, a key aspect that should be included in the definition of the theoretical problem is the interaction between the carbon structure and the substrate [99,100]. In fact, quantum transport calculations for GNR structures epitaxially grown on SiC substrates have shown that their conductive behavior can significantly vary with respect to their ideally free-standing counterparts [101]. From a methodological point of view, multidisciplinary approaches could evidence important aspects of device operation for such systems. As an example, answers to simple questions like, “how stable is a graphene nanoribbon device at high temperatures?”, could be affronted within combined molecular dynamics and quantum transport calculations for the verification of conductance fluctuations with respect to defect metastability. Finally it should be noted that a further effort in order to implement scaling and optimization techniques in quantum transport codes is necessary for a more efficient application of theoretical models over experimental data.

The authors would like to acknowledge the European Science Foundation (ESF) under the EUROCORES Programme EuroGRAPHENE CRP GRAPHIC-RF for partial financial support.

References

1. A. Aviram, M.A. Ratner, Chem. Phys. Lett. **29**, 277 (1974)
2. S. Iijima, Nature **354**, 56 (1991)
3. R.H. Baughman, A.A. Zakhidov, W.A. de Heer, Science **297**, 787 (2002)
4. P. Avouris, Z. Chen, V. Perebeinos, Nature Nanotechnol. **2**, 605 (2007)
5. N.D. Mermin, H. Wagner, Phys. Rev. Lett. **17**, 1133 (1966)
6. N.D. Mermin, Phys. Rev. **176**, 250 (1968)
7. K.S. Novoselov, A.K. Geim, S.V. Morozov, D. Jiang, Y. Zhang, S.V. Dubonos, I.V. Grigorieva, A.A. Firsov, Science **306**, 666 (2004)
8. A.K. Geim, K.S. Novoselov, Nature Mater. **6**, 183 (2007)
9. Y. Son, M.L. Cohen, S.G. Louie, Phys. Rev. Lett. **97**, 216803 (2006)
10. Y. Zhang, T. Tang, C. Girit, Z. Hao, M.C. Martin, A. Zettl, M.F. Crommie, Y.R. Shen, F. Wang, Nature **459**, 820 (2009)
11. P. Gava, M. Lazzeri, A.M. Saitta, F. Mauri, Phys. Rev. B **79**, 165431 (2009)
12. S.Y. Zhou, G. Gweon, A.V. Fedorov, P.N. First, W.A. de Heer, D. Lee, F. Guinea, A.H. Castro Neto, A. Lanzara, Nature Mater. **6**, 916 (2007)
13. S. Kim, J. Ihm, H.J. Choi, Y. Son, Phys. Rev. Lett. **100**, 176802 (2008)
14. D.W. Boukhvalov, M.I. Katsnelson, Phys. Rev. B **78**, 085413 (2008)
15. B. Biel, F. Triozon, X. Blase, S. Roche, Nano Lett. **9**, 2725 (2009)
16. I. Deretzis, G. Fiori, G. Iannaccone, A. La Magna, Phys. Rev. B **81**, 085427 (2010)
17. G. Cocco, E. Cadelano, L. Colombo, Phys. Rev. B **81**, 241412 (2010)
18. V.M. Pereira, A.H. Castro Neto, Phys. Rev. Lett. **103**, 046801 (2009)
19. J.R. Heath, Q. Zhang, S.C. O’Brien, R.F. Curl, H.W. Kroto, R.E. Smalley, J. Am. Chem. Soc. **109**, 359 (1987)
20. V. Scuderi, S. Scalese, S. Bagiante, G. Compagnini, L. D’Urso, V. Privitera, Carbon **47**, 2134 (2009), ISSN 0008-6223
21. A. La Magna, I. Deretzis, V. Privitera, Eur. Phys. J. B **70**, 311 (2009)
22. J.C. Meyer, C. Kisielowski, R. Erni, M.D. Rossell, M.F. Crommie, A. Zettl, Nano Lett. **8**, 3582 (2008)
23. Y. Lin, K.A. Jenkins, A. Valdes-Garcia, J.P. Small, D.B. Farmer, P. Avouris, Nano Lett. **9**, 422 (2009)
24. S. Datta, *Electronic transport in mesoscopic systems* (Cambridge University Press, 1995)
25. A. La Magna, I. Deretzis, G. Forte, R. Pucci, Phys. Rev. B **78**, 153405 (2008)
26. A.H. Castro Neto, F. Guinea, N.M.R. Peres, K.S. Novoselov, A.K. Geim, Rev. Mod. Phys. **81**, 109 (2009)
27. S. Dubois, Z. Zanolli, X. Declerck, J. Charlier, Eur. Phys. J. B **72**, 1 (2009)
28. V.M. Pereira, J.M.B. Lopes Dos Santos, A.H. Castro Neto, Phys. Rev. B **77**, 115109 (2008)
29. S. Datta, *Quantum transport: atom to transistor* (Cambridge University Press, 2005)
30. I. Deretzis, A. La Magna, Nanotechnology **17**, 5063 (2006)
31. C. Thomsen, S. Reich, J. Maultzsch, *Carbon Nanotubes: Basic Concepts and Physical Properties* (Wiley-VCH Verlag GmbH, 2007)
32. M. Fujita, K. Wakabayashi, K. Nakada, K. Kusakabe, J. Phys. Soc. Jpn **65**, 1920 (1996)
33. K. Nakada, M. Fujita, G. Dresselhaus, M.S. Dresselhaus, Phys. Rev. B **54**, 17954 (1996)
34. H. Zheng, Z.F. Wang, T. Luo, Q.W. Shi, J. Chen, Phys. Rev. B **75**, 165414 (2007)
35. B. Huang, F. Liu, J. Wu, B.L. Gu, W. Duan, Phys. Rev. B **77**, 153411 (2008)
36. T. Wassmann, A.P. Seitsonen, A.M. Saitta, M. Lazzeri, F. Mauri, Phys. Rev. Lett. **101**, 096402 (2008)
37. O.V. Yazyev, M.I. Katsnelson, Phys. Rev. Lett. **100**, 047209 (2008)

38. R. Peierls, *Quantum Theory of Solids* (Oxford University Press, 1955)
39. E. Cazzanelli, M. Castriota, L.S. Caputi, A. Cupolillo, C. Giallombardo, L. Papagno, *Phys. Rev. B* **75**, 121405 (2007)
40. A.J. Heeger, S. Kivelson, J.R. Schrieffer, W. Su, *Rev. Mod. Phys.* **60**, 781 (1988)
41. Ž. Crljen, G. Baranović, *Phys. Rev. Lett.* **98**, 116801 (2007)
42. M. Paulsson, [arXiv:cond-mat/0210519](https://arxiv.org/abs/cond-mat/0210519) (2002)
43. F. Zahid, M. Paulsson, S. Datta, *Electrical conduction in molecules, chapter in advanced semiconductors and organic nano-techniques*, edited by H. Morkoc (Academic Press, 2003), ISBN: 0-12-507060-8
44. M.P. Anantram, M.S. Lundstrom, D.E. Nikonov, [arXiv:cond-mat/0610247](https://arxiv.org/abs/cond-mat/0610247) (2006)
45. Y. Imry, R. Landauer, *Rev. Mod. Phys. Suppl.* **71**, 306 (1999)
46. S. Datta, *Nanoelectronic devices: A unified view* (Oxford Handbook on Nanoscience and Nanotechnology: Frontiers and Advances, 2008)
47. S. Datta, *Superlattices Microstruct.* **28**, 253 (2000)
48. D. Kienle, J.I. Cerda, A.W. Ghosh, *J. Appl. Phys.* **100**, 043714 (2006)
49. I.N. Levine, *Quantum Chemistry* (Pearson Education International, 2009)
50. G. Fiori, G. Iannaccone, G. Klimeck, *IEEE Trans. Nanotechnol.* **6**, 475 (2007)
51. D. Petersen, S. Li, K. Stokbro, H. Sørensen, P. Hansen, S. Skelboe, E. Darve, *J. Comput. Phys.* **228**, 5020 (2009)
52. D. Petersen, H. Sørensen, P. Hansen, S. Skelboe, K. Stokbro, *J. Comput. Phys.* **227**, 3174 (2008)
53. M.P.L. Sancho, J.M.L. Sancho, J.M.L. Sancho, J. Rubio, *J. Phys. F Met. Phys.* **15**, 851 (1985)
54. M. Brandbyge, J. Mozos, P. Ordejón, J. Taylor, K. Stokbro, *Phys. Rev. B* **65**, 165401 (2002)
55. G. Vignale, M. di Ventra, *Phys. Rev. B* **79**, 014201 (2009)
56. J.M. Carlsson, M. Scheffler, *Phys. Rev. Lett.* **96**, 046806 (2006)
57. M. Hjort, S. Stafström, *Phys. Rev. B* **61**, 14089 (2000)
58. J.J. Palacios, J. Fernández-Rossier, L. Brey, *Phys. Rev. B* **77**, 195428 (2008)
59. O.V. Yazyev, L. Helm, *Phys. Rev. B* **75**, 125408 (2007)
60. F. Banhart, J. Kotakoski, A.V. Krasheninnikov, *ACS Nano* **5**, 26 (2011)
61. T.C. Li, S. Lu, *Phys. Rev. B* **77**, 085408 (2008)
62. D.A. Bahamon, A.L.C. Pereira, P.A. Schulz, *Phys. Rev. B* **82**, 165438 (2010)
63. L. Chico, L.X. Benedict, S.G. Louie, M.L. Cohen, *Phys. Rev. B* **54**, 2600 (1996)
64. I. Deretzis, G. Forte, A. Grassi, A. La Magna, G. Piccitto, R. Pucci, *J. Phys.: Condens. Matter* **22**, 095504 (2010)
65. H.J. Choi, J. Ihm, S.G. Louie, M.L. Cohen, *Phys. Rev. Lett.* **84**, 2917 (2000)
66. B. Biel, X. Blase, F. Triozon, S. Roche, *Phys. Rev. Lett.* **102**, 096803 (2009)
67. A. La Magna, I. Deretzis, G. Forte, R. Pucci, *Phys. Rev. B* **80**, 195413 (2009)
68. A. López-Bezanilla, F. Triozon, S. Roche, *Nano Lett.* **9**, 2537 (2009)
69. A. López-Bezanilla, F. Triozon, S. Latil, X. Blase, S. Roche, *Nano Lett.* **9**, 940 (2009)
70. A. La Magna, I. Deretzis, G. Forte, R. Pucci, *Phys. Status Solidi (c)* **7**, 1246 (2010)
71. N. Gorjizadeh, A.A. Farajian, Y. Kawazoe, *Nanotechnology* **20**, 015201 (2009)
72. J. Chen, C. Jang, S. Adam, M.S. Fuhrer, E.D. Williams, M. Ishigami, *Nature Phys.* **4**, 377 (2008)
73. M.P. Anantram, T.R. Govindan, *Phys. Rev. B* **58**, 4882 (1998)
74. P.W. Anderson, D.J. Thouless, E. Abrahams, D.S. Fisher, *Phys. Rev. B* **22**, 3519 (1980)
75. Y. Lin, V. Perebeinos, Z. Chen, P. Avouris, *Phys. Rev. B* **78**, 161409 (2008)
76. F. Léonard, J. Tersoff, *Phys. Rev. Lett.* **83**, 5174 (1999)
77. A.A. Odintsov, *Phys. Rev. Lett.* **85**, 150 (2000)
78. F. Léonard, J. Tersoff, *Phys. Rev. Lett.* **84**, 4693 (2000)
79. S. Heinze, J. Tersoff, R. Martel, V. Derycke, J. Appenzeller, P. Avouris, *Phys. Rev. Lett.* **89**, 106801 (2002)
80. A. Svizhenko, M.P. Anantram, *Phys. Rev. B* **72**, 085430 (2005)
81. I. Deretzis, A. La Magna, *Physica, E, Low-Dimens. Syst. Nanostruct.* **40**, 2333 (2008)
82. I. Deretzis, G. Fiori, G. Iannaccone, A. La Magna, *Phys. Rev. B* **82**, 161413 (2010)
83. J. Guo, S. Datta, M. Lundstrom, M.P. Anantram, *Int. J. Multiscale Computational Engineering* **2**, 257 (2004)
84. Y. Lin, V. Perebeinos, Z. Chen, P. Avouris, *Phys. Rev. B* **78**, 161409 (2008)
85. Z. Chen, J. Appenzeller, J. Knoch, Y. Lin, P. Avouris, *Nano Lett.* **5**, 1497 (2005)
86. M.P. Anantram, S. Datta, Y. Xue, *Phys. Rev. B* **61**, 14219 (2000)
87. M. Vanin, J.J. Mortensen, A.K. Kelkkanen, J.M. Garcia-Lastra, K.S. Thygesen, K.W. Jacobsen, *Phys. Rev. B* **81**, 081408 (2010)
88. J.A. Rodríguez-Manzo et al., *Proc. Nat. Acad. Sci.* **106**, 4591 (2009)
89. F. Bussolotti, L. D'Ortenzi, V. Grossi, L. Lozzi, S. Santucci, M. Passacantando, *Phys. Rev. B* **76**, 125415 (2007)
90. F. Zahid, M. Paulsson, E. Polizzi, A.W. Ghosh, L. Siddiqui, S. Datta, *J. Chem. Phys.* **123**, 064707 (2005)
91. I. Deretzis, A. La Magna, *Appl. Phys. Lett.* **91**, 163111 (2007)
92. I. Deretzis, A. La Magna, *J. Chem. Phys.* **128**, 164706 (2008)
93. I. Deretzis, A.L. Magna, *Mater. Sci. Semiconduc. Process.* **11**, 190 (2008)
94. L.D. Landau, *Phys. Z. Sowjetunion* **3**, 664 (1933)
95. A. La Magna, I. Deretzis, *Phys. Rev. Lett.* **99**, 136404 (2007)
96. M. Galperin, M.A. Ratner, A. Nitzan, A. Troisi, *Science* **319**, 1056 (2008)
97. M. Galperin, M.A. Ratner, A. Nitzan, *Nano Lett.* **5**, 125 (2005)
98. N.D. Mermin, *Phys. Rev.* **137**, 1441 (1965)
99. I. Deretzis, A. La Magna, *Appl. Phys. Lett.* **98**, 023113 (2011)
100. Y. Zhou, M.W. Wu, *Phys. Rev. B* **82**, 085304 (2010)
101. I. Deretzis, A. La Magna, *Appl. Phys. Lett.* **95**, 063111 (2009)